Bridgeless Hybrid-Mode Zeta-Based Inverter: Dynamic Modeling and Control

Byeongcheol Han, *Member, IEEE*, Seung-Won Jo, *Student Member, IEEE*, Nam-Gyeong Kim, *Student Member, IEEE*, Jih-Sheng Lai, *Life Fellow, IEEE*, and Minsung Kim, *Senior Member, IEEE*

***Abstract*—In this article, we present a bridgeless hybrid-mode Zeta inverter for distributed energy systems. We integrate the secondary diode of the conventional unfolding-type Zeta inverter into one of diagonal pairs of the secondary-side switches in a bridgeless Zeta inverter. This structure decreases the number of active power components and provides naturally well distributed loss at the body diodes of the secondary-side switches over one cycle of grid voltage, and as a result, increases both output power transfer and reliability. To attain medium-high power capacity with appropriate size of magnetic components, the bridgeless Zeta inverter operates in both discontinuous conduction mode (DCM) and continuous conduction mode (CCM). However, control of the proposed inverter is difficult because of the distinct system dynamics caused by the operations in DCM and CCM. To deal with this control problem, we first identify the mode boundaries and, corresponding to each mode, develop a dynamic model to design a controller. Then, we propose to use a feedback controller plus a feedforward controller supplemented with a repetitive controller that uses a phase-lead compensator. Experimental results using a 300-W prototype demonstrate the feasibility and effectiveness of the proposed modeling and control approach.**

***Index Terms*—Bridgeless inverter, continuous conduction mode (CCM), discontinuous conduction mode (DCM), phase-lead compensator, repetitive control, Zeta topology.**

I. Introduction

INCREASING preference toward more efficient distributed energy systems is stimulating the demand for module-integrated converters (MICs). Each MIC is mounted on a single energy module, captures electric power from it, and delivers the power to the utility grid. MICs enable individual operation of each energy module, such as photovoltaic/thermoelectric module; this arrangement reduces power losses caused by the mismatch between the modules. Recently, the Internet of Things [1] have been embedded in MICs to facilitate collection of remote diagnostics for each module. These MICs must meet grid code requirements and at the same time should achieve low installation cost per watt, compact size, and high power conversion efficiency [2]–[6]. To meet these requirements, appropriate topology must be selected.

Among the various single-stage dc–ac circuit topologies, unfolding-type inverters are considered attractive for MICs. In these topologies, the dc–dc converter converts the dc voltage to the rectified ac voltage and the unfolding bridge unfolds the rectified ac voltage to the ac voltage. This arrangement eliminates the inverter stage and reduces the dc-link capacitance, compared to the conventional two-stage inverters. Thus, the unfolding-type inverters feature high power density, long lifetime, and simplified control. Usually, unfolding-type inverters have been developed in flyback topology. Unfolding-type flyback inverters have the advantages of small number of components, low cost, and high conversion efficiency [7]–[9]. However, a main concern with this topology is a limited output power. A voltage spike at the primary-side switch results in difficulty in increasing the output power. To reduce this spike, an active-clamp circuit [10]–[12] has been added to the conventional flyback inverters. Recently, a flyback inverter that operates in continuous conduction mode (CCM) [13]–[15] has also been proposed. Despite these efforts, the operating power range of unfolding-type flyback inverters is limited to 200 W due to the high peak current flowing through the active and passive devices.

Unfolding-type Zeta inverters have been presented [16] as a method to further increase the power level. They inherit the characteristics of Zeta topology, have buck–boost capability, so they function under a wide input/output voltage range. An important feature of the Zeta inverters is that the inherent output inductor generates continuous output current, and thereby further reduces the ripple of the current that flows through the secondary-side diode compared to the inverter that uses flyback topology. However, these unfolding-type Zeta inverters must use an unfolding bridge at the grid side. This bridge incurs a localized heat management problem, followed by high conduction losses. The high junction temperature degrades the electrical

Manuscript received June 28, 2020; revised October 1, 2020; accepted November 18, 2020. Date of publication November 24, 2020; date of current version February 5, 2021. This work was supported by the Basic Science Research Program through the National Research Foundation of Korea funded by the Ministry of Education under Grant 2018R1D1A1B07044999. Recommended for publication by Associate Editor J. Rabkowski. *(Corresponding author: Minsung Kim.)*

Byeongcheol Han is with the School of Electronics Engineering and with the School of Electronic and Electrical Engineering, Kyungpook National University, Daegu 41566, South Korea (e-mail: hbychol@knu.ac.kr).

Seung-Won Jo, Nam-Gyeong Kim, and Minsung Kim are with the Division of Electronics and Electrical Engineering, Dongguk University, Seoul 04620, South Korea (e-mail: vsw3127@naver.com; wgx010@naver.com; mkim@dgu.ac.kr).

Jih-Sheng Lai is with the Future Energy Electronics Center, Virginia Polytechnic Institute and State University, Blacksburg, VA 24061 USA (e-mail: laijs@vt.edu).

Color versions of one or more of the figures in this article are available at https://doi.org/10.1109/TPEL.2020.3040113.

Digital Object Identifier 10.1109/TPEL.2020.3040113

characteristics of active power components and increases the metal migration, which causes accelerated aging and increased failure rate [17]. Another challenge of this topology is that the diode on the secondary side of the transformer conducts over one cycle of grid voltage, and this trait complicates the task of heat management. To alleviate this problem, differential-mode Zeta inverters have been presented for single-phase and three-phase utility grids [18]–[20]. These inverters are made based on multiple modules, which are connected in parallel at the dc side and connected in series at the ac side. Compared to the conventional unfolding-type Zeta inverters, these differential-mode Zeta inverters increase the efficiency of the circuit by eliminating the unfolding bridge and its conduction loss in the ac line current path. However, the differential-mode Zeta inverter circuit is not fully utilized over the entire ac-line cycle: one part of it is utilized over the positive half-cycle and the other part is utilized over the negative half-cycle. The use of these two independent circuits leads to the need for a large number of power components. To address these drawbacks, the single-stage structure has been investigated for the Zeta converter [21]. This structure consists of single switch at the primary side, one center-tapped transformer, and single inductor ended structure with two half-bridge circuits. This configuration can further decrease the number of required power components. However, only one of the body diodes in the secondary-side switches conducts depending on the polarity of the grid voltage over one cycle of the grid voltage, so heat management is still a problem. In addition, the center-tapped transformer may increase the development cost; the inequality of the two secondary windings in the center-tapped transformer would cause a leakage inductance imbalance, which could cause imbalanced resonant current flow through the capacitor at every half switching cycle. Furthermore, the control accuracy of the bridgeless Zeta inverter has been tested under the grid-forming mode. When the inverter operates in grid-connected mode, the transfer function of the bridgeless Zeta inverter has right-half-plane (RHP) zeros, and also suffers from grid voltage disturbance when connected to the utility grid. The conventional proportional-integral (PI) control scheme coupled with feedforward controller cannot accomplish satisfactory tracking accuracy, so the topology has poor power quality and high total harmonic distortion (THD) at the output current.

This article proposes a hybrid-mode bridgeless Zeta inverter and presents its dynamic modeling and control. This inverter does not have a secondary-side diode; instead, one of diagonal pairs of the secondary-side switches operates depending on the polarity of the grid voltage over one cycle of the grid voltage. Because of this aspect, the loss accumulated at the original secondary-side diode is distributed to all body diodes of the secondary-side switches. By means of balanced loss distribution, the proposed inverter achieves easy heat management, increased output power transfer capability, and increased reliability. To achieve medium-high power capacity with appropriate size of magnetic components, the proposed inverter operates in discontinuous conduction mode (DCM) during the low instantaneous power region, and in CCM during the high instantaneous power region. However, control of the proposed inverter is difficult because DCM and CCM have distinct system dynamics. To solve this problem, we first identify the mode boundaries, then develop dynamic models that correspond to DCM and CCM. We apply a repetitive controller (RC) to achieve zero steady-state tracking error under the grid voltage disturbance. Different phase-lead compensators in the RC compensate for different phase lags incurred by distinct system dynamics. Based on the dynamic models, we determine the nominal duty ratios and control parameters for feedback controllers, RCs, and phase-lead compensators. Experimental tests using a 300-W prototype demonstrate the validity of this design.

The remainder of this article is arranged as follows. Section II presents the dynamic modeling of hybrid-mode Zeta inverter, then Section III gives its steady-state analysis. Section IV proposes a control scheme for the hybrid-mode Zeta inverter. Section V presents experimental results and discussion. Finally, Section VI concludes this article.

II. Problem Formulation

The unfolding-type Zeta inverter [16] [see Fig. 1(a)] requires the secondary-side diode, which accumulates a large loss during the grid period. The single-stage Zeta inverter [21] [see Fig. 1(b)] has no secondary diode, so the accumulated loss at the original secondary-side diode is distributed among the body diodes of the two switches; halving the accumulated loss can simplify the design of the heat sink, but the center-tapped transformer increases the development cost of the inverter. In the proposed bridgeless Zeta inverter [see Fig. 1(c)], the accumulated loss is separated into four switches at the secondary side. A quarter of the heat can simplify the design of the heat sink further or even remove the heat sink. Moreover, the proposed inverter does not require a center-tapped transformer, which results in reduction of the development cost of the circuit.

The bridgeless Zeta-based inverter [see Fig. 1(c)] consists of inductors L_1, input capacitor C_{in}, primary-side switch S_1, secondary-side switches $S_2 - S_5$, filter capacitor C_o, filter inductor L_f, transformer T with turns ratio $n = N_s/N_p$, and its magnetizing inductance L_m. The primary switch S_1 operates with high frequency, and the secondary switches S_2–S_5 commute at a grid frequency f_g. The body-diode of S_4 or S_5 works as the secondary-side diode of the conventional Zeta converter. An LCL-type filter suppresses the harmonic components in the grid current as a low-pass filter (LPF), and thereby yields low continuous current ripple at the output side. The primary switch operates with a variable duty cycle to generate sinusoidal ac output, whereas the secondary switches S_2–S_5 commute at f_g depending on the grid voltage polarity: S_3 and S_4 are turned ON during the positive half-cycle of the grid voltage, and OFF during the negative half-cycle, whereas S_2 and S_5 are turned ON during the negative half-cycle and OFF during the negative half-cycle. As a result, the proposed inverter transforms dc input power to ac output power in a single step without any additional transformer winding. The proposed inverter works as an isolated Zeta converter, so it can achieve step-up and step-down by the operation of only five switches.

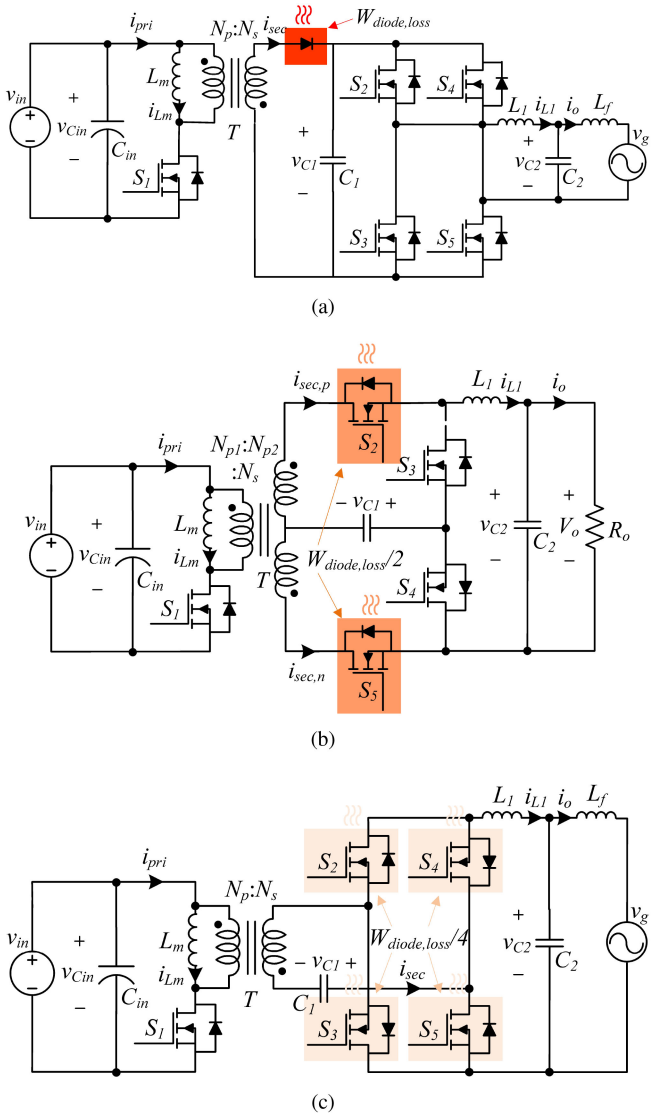

Fig. 1. Circuit diagrams of the Zeta topology based inverters. $W_{\text{diode,loss}} = \int_0^{T_g} P_{\text{diode,loss}}(t)dt$ is the energy loss occurred during a grid period T_g; $P_{\text{diode,loss}}(t)$ is the conduction loss occurred at the secondary diode during a switching period. (a) Unfolding-type Zeta inverter [16]. (b) Single-stage Zeta inverter [21]. (c) Proposed bridgeless Zeta-based inverter.

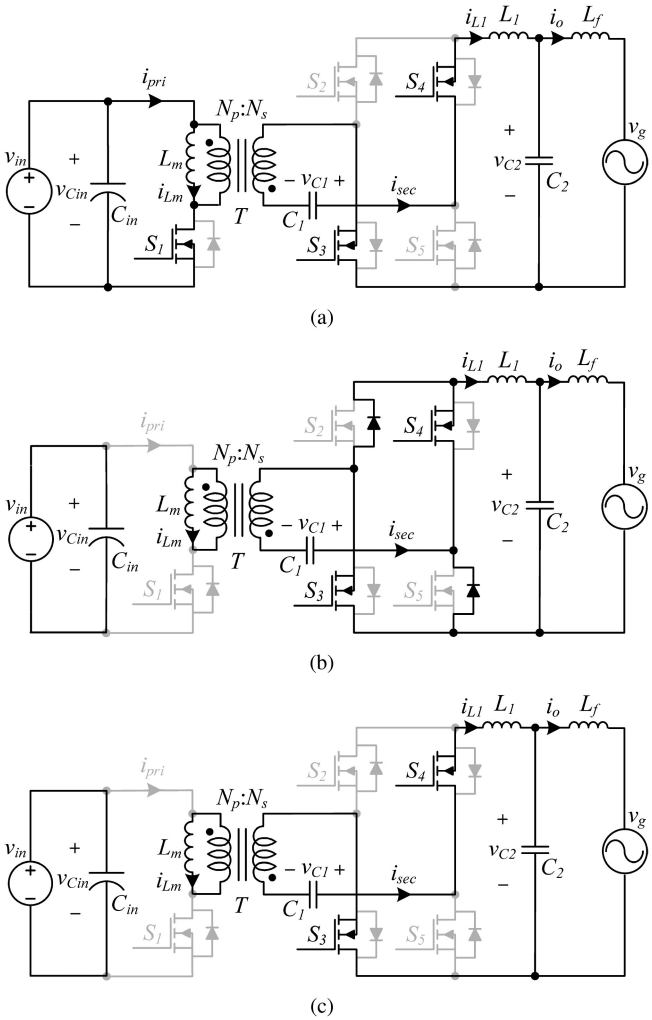

Fig. 2. Operating phases of the proposed bridgeless Zeta-based inverter. (a) Phase I. (b) Phase II. (c) Phase III.

A. Operation Principle

The operation principles are based on the assumption that the leakage inductance of the transformer T is neglected; the ith switch ($i = 1, ...5$) consists of an ideal switch S_i and a body diode D_{Si}; the capacitance of the input capacitor C_{in} is sufficiently large, so input voltage V_{in} is constant. The proposed inverter has two modes, CCM and DCM depending on the operating point and inductances (L_m and L_1). This section will analyze steady-state operation principles in CCM and DCM within one switching cycle T_s.

During the positive half-cycle of the grid voltage, the circuit experiences three phases per switching period (see Fig. 2), which are as follows.

1) Phase I (S_1, S_3, and S_4 ON; D_{S2} and D_{S5} OFF): The current flowing through D_{S2} and D_{S5} is blocked during this interval. The current flowing through L_m increases and the energy is transferred to C_1. Meanwhile, the energy stored in C_1 is transferred to the grid.

2) Phase II (S_3, S_4, D_{S2}, and D_{S5} ON; S_1 OFF): D_{S2} and D_{S5} conduct during this interval. The current flowing through L_m decreases and the stored energy in L_m is transferred to C_1. Meanwhile, the energy stored in C_1 is transferred to the grid. When the circuit operates in CCM, its operation returns to phase I. In contrast, when the circuit operates in DCM, the currents flowing though L_m and L_1 continue to decrease and the current flowing through L_1 becomes negative.

3) Phase III (S_3 and S_4 ON; S_1, D_{S2}, and D_{S5} OFF): After the current flowing through D_{S2} and D_{S5} reaches zero, it becomes zero, then the dc offset current I_X flows through the circuit in DCM.

During the negative half-cycle of the grid voltage, the circuit experiences the same phases per switching period. The difference lies in that diagonal switch pairs at the secondary side operate in reverse, i.e., S_2 and S_5 are turned ON; S_3 and S_4 are turned OFF. The theoretical waveforms of the proposed inverter

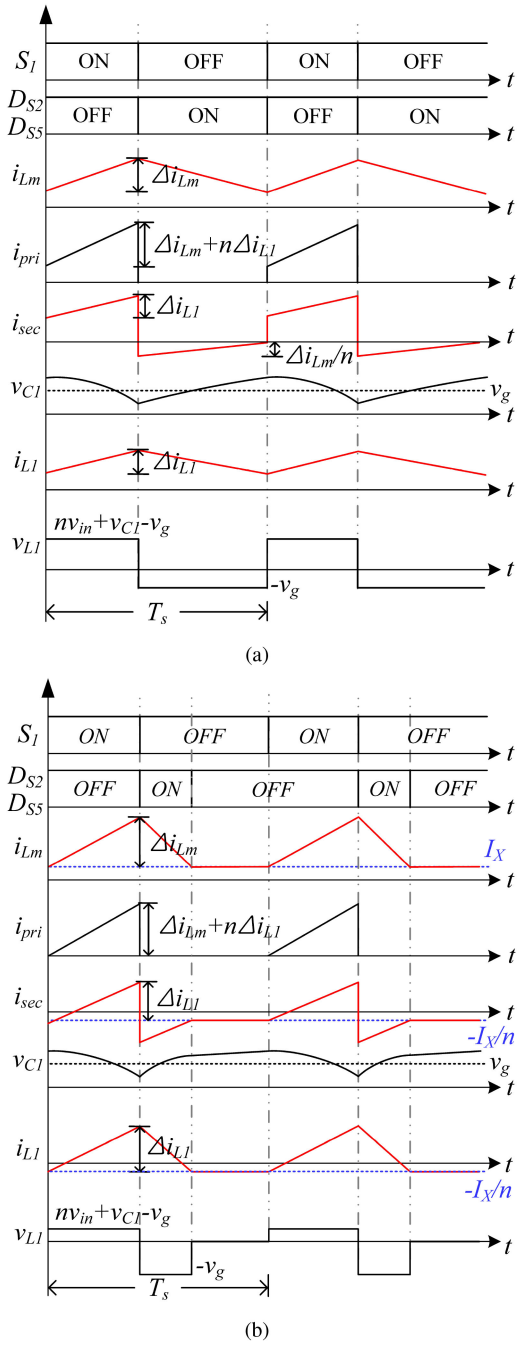

Fig. 3. Theoretical waveforms of voltages and currents when $v_g > 0$. Δi_{Lm} and i_{L1} are the ripples of the magnetizing current and the current flowing through L_1, respectively. (a) In CCM. (b) In DCM.

in a switching cycle during the positive half-cycle of the grid voltage are shown in Fig. 3.

B. Dynamic Modeling

The operation principle of the proposed bridgeless Zeta inverter is essentially the same during both positive and negative half-cycles of the grid voltage, so this section analyzes only the dynamic model of this inverter during the positive half-cycle.

The proposed inverter undergoes phases I, II, and III during DCM, but only phases I and II during CCM. Based on state-space equations of three phases, the state-space averaging method yields the average model (1) and (2) where $\mathbf{x}(t) = [i_{L_m}(t), v_{C_1}(t), i_{L_1}(t), v_{C_2}(t), i_o(t)]^T$ is the state vector; $y(t) = i_o(t)$ is the output; duty ratio $d_1(t)$ is the ratio of the ON-time of S_1; duty ratio $d_2(t)$ is the ratio of the ON-time of the body diodes in S_2 and S_5, and $d_2(t) = 1 - d_1(t)$ in CCM and $d_2(t)$ in DCM (see Section III-A); $M_1(t) = \frac{1-d_1(t)-d_2(t)}{L_{1m}}$; $M_2(t) = \frac{d_1(t)+d_2(t)}{L_1}$; $L_{1m} = L_1 + n^2 L_m$; and r_{L_1}, r_{L_f}, and r_{C_2} are the parasitic resistances of L_1, L_f, and C_2, respectively.

Linearizing the average model in (1) and (2), as shown at the bottom of the next page, yields the small-signal models for DCM and CCM.

DCM

$$\dot{\hat{\mathbf{x}}}(t) = \begin{bmatrix} \frac{\partial F_1}{\partial \hat{x}_1} & \frac{\partial F_1}{\partial \hat{x}_2} & \frac{\partial F_1}{\partial \hat{x}_3} & \frac{\partial F_1}{\partial \hat{x}_4} & -n\bar{M}_1 r_{C_2} \\ \frac{1-D_1}{nC_1} & 0 & -\frac{D_1}{C_1} & 0 & 0 \\ \frac{\partial F_3}{\partial \hat{x}_1} & \frac{\partial F_3}{\partial \hat{x}_2} & \frac{\partial F_3}{\partial \hat{x}_3} & \frac{\partial F_3}{\partial \hat{x}_4} & r_{C_2}\left(\bar{M}_1 + \bar{M}_2\right) \\ 0 & 0 & \frac{1}{C_2} & 0 & -\frac{1}{C_2} \\ 0 & 0 & \frac{r_{C_2}}{L_f} & \frac{1}{L_f} & -\frac{r_{L_f}+r_{C_2}}{L_f} \end{bmatrix} \hat{\mathbf{x}}(t) + \begin{bmatrix} \frac{\partial F_1}{\partial \hat{d}_1} \\ -\frac{I_{Lm}}{nC_1} - \frac{I_{L_1}}{C_1} \\ \frac{\partial F_3}{\partial \hat{d}_1} \\ 0 \\ 0 \end{bmatrix} \hat{d}_1(t) \tag{3}$$

$$\hat{y}(t) = \begin{bmatrix} 0 & 0 & 0 & 0 & 1 \end{bmatrix} \hat{\mathbf{x}}(t) \tag{4}$$

CCM

$$\dot{\hat{\mathbf{x}}}(t) = \begin{bmatrix} 0 & -\frac{1-D_1}{nL_m} & 0 & 0 & 0 \\ \frac{1-D_1}{nC_1} & 0 & -\frac{D_1}{C_1} & 0 & 0 \\ 0 & \frac{D_1}{L_1} & -\frac{r_{L_1}+r_{C_2}}{L_1} & -\frac{1}{L_1} & \frac{r_{C_2}}{L_1} \\ 0 & 0 & \frac{1}{C_2} & 0 & -\frac{1}{C_2} \\ 0 & 0 & \frac{r_{C_2}}{L_f} & \frac{1}{L_f} & -\frac{r_{L_f}+r_{C_2}}{L_f} \end{bmatrix} \cdot \hat{\mathbf{x}}(t) + \begin{bmatrix} \frac{V_{\text{in}}}{L_m} + \frac{V_{C_1}}{nL_m} \\ -\frac{I_{Lm}}{nC_1} - \frac{I_{L_1}}{C_1} \\ \frac{V_{C_1}}{L_1} + \frac{nV_{\text{in}}}{L_1} \\ 0 \\ 0 \end{bmatrix} \hat{d}_1(t) \tag{5}$$

$$\hat{y}(t) = \begin{bmatrix} 0 & 0 & 0 & 0 & 1 \end{bmatrix} \hat{\mathbf{x}}(t) \tag{6}$$

where $\hat{\mathbf{x}}(t) = [\hat{i}_{L_m}(t), \hat{v}_{C_1}(t), \hat{i}_{L_1}(t), \hat{v}_{C_2}(t), \hat{i}_o(t)]^T$, $\hat{y}(t) = \hat{i}_o(t)$, and $\hat{d}(t)$ are, respectively, the incremental variations of $\mathbf{x}(t) = [i_{L_m}(t), v_{C_1}(t), i_{L_1}(t), v_{C_2}(t), i_o(t)]^T$, $y(t) = i_o(t)$, and $d_1(t)$; I_{L_m}, V_{C_1}, I_{L_1}, V_{C_2}, I_o, D_1, and D_2 are, respectively, the values at the operating point of $i_{L_m}(t)$, $v_{C_1}(t)$, $i_{L_1}(t)$, $V_{C_2}(t)$, $i_o(t)$, $d_1(t)$, and $d_2(t)$; $\bar{M}_1 = \frac{1-D_1-D_2}{L_{1m}}$; $\bar{M}_2 = \frac{D_1+D_2}{L_1}$; F_i, $\frac{\partial F_i}{\partial \hat{x}_j}$, and $\frac{\partial F_i}{\partial \hat{d}_1}$ for $i = 1, 3$ and $j = 1, ..., 4$ (see Appendix A).

From these small-signal models for DCM and CCM, the transfer functions from the control input to the output can be derived as follows:

DCM

$$G_{id\_\mathrm{DCM}}(s)=\frac{\hat{i}_o(s)}{\hat{d}_1(s)}=\frac{a_1s^3+a_2s^2+a_3s+a_4}{b_1s^5+b_2s^4+b_3s^3+b_4s^2+b_5s+b_6} \tag{7}$$

CCM

$$G_{id\_\mathrm{CCM}}(s)=\frac{\hat{i}_o(s)}{\hat{d}_1(s)}=\frac{c_1s^3+c_2s^2+c_3s+c_4}{e_1s^5+e_2s^4+e_3s^3+e_4s^2+e_5s+e_6} \tag{8}$$

with derived parameters a_i and c_i for $i=1,...,4$ and b_j and e_j for $j=1,...,6$ (see Appendix B). Analysis of the aforementioned small-signal models reveals that $G_{id\_\mathrm{DCM}}(z)$ has five left-half-plane (LHP) poles, one RHP zero, and two LHP zeros, whereas $G_{id\_\mathrm{CCM}}(z)$ has five LHP poles, two RHP zeros, and one LHP zero. To develop the controller in the discrete-time domain, the bilinear transformation method with the sampling period T_s converts the continuous-time transfer functions (7) and (8) to the discrete-time transfer functions $G_{id\_\mathrm{DCM}}(z)$, $G_{id\_\mathrm{CCM}}(z)$.

III. Steady-State Analysis

A. DC-Offset Current Calculation

When the bridgeless Zeta inverter operates in DCM, dc-offset currents flow through L_m and L_1. These currents differentiate the Zeta inverter that operates in DCM from other DCM inverters, such as flyback and nonisolated buck–boost inverters. Considering that inductor currents exhibit triangular waveforms [see Fig. 3(b)], the average currents flowing L_m and L_1 can be described as

$$I_{L_m}=\frac{1}{T_s}\int_0^{T_s}i_{L_m}(t)dt=I_X+\frac{v_{\mathrm{in}}d_1\left(d_1+d_2\right)T_s}{2L_m} \tag{9}$$

$$\begin{aligned}I_{L_1}&=\frac{1}{T_s}\int_0^{T_s}i_{L_1}(t)dt\\&=-\frac{I_X}{n}+\frac{\left(nv_{\mathrm{in}}+v_{C_1}-|v_{C_2}|\right)d_1\left(d_1+d_2\right)T_s}{2L_1}\end{aligned} \tag{10}$$

where I_X is a dc-offset current, the value of which depends on duty ratio d_2.

Eliminating I_X in (9) and (10) yields

$$d_2=\frac{2\left(I_{L_m}+nI_{L_1}\right)}{d_1T_s\left(\frac{v_{\mathrm{in}}}{L_m}+\frac{n}{L_1}\left(nv_{\mathrm{in}}+v_{C_1}-|v_{C_2}|\right)\right)}-d_1. \tag{11}$$

By substituting (11) into (10) [or (9)], the dc-offset current I_X can be obtained as

$$I_X=\frac{\left(I_{L_m}+nI_{L_1}\right)\left(nv_{\mathrm{in}}+v_{C_1}-v_{C_2}\right)}{\frac{v_{\mathrm{in}}L_1}{nL_m}+nv_{\mathrm{in}}+v_{C_1}-v_{C_2}}-nI_{L_1}. \tag{12}$$

The steady-state voltages v_{C_1} and $|v_{C_2}|$ are computed as $|v_g|$ by the inductor volt-second balance law. Then, simplifying (12) yields

$$I_X=\frac{n^2L_mI_{L_m}-nL_1I_{L_1}}{L_1+n^2L_m}. \tag{13}$$

B. Nominal Duty Ratio Derivation

Assuming that the inverter circuit is lossless and it operates in quasi-steady-state during the switching period, the power balance equations in both CCM and DCM regions are

$$V_{\mathrm{in}}I_{\mathrm{in}}=V_{g,\mathrm{rms}}\bar{I}_{o,\mathrm{rms}}=P_o \tag{14}$$

$$V_{\mathrm{in}}I_{\mathrm{pri}}=V_g\bar{I}_o=2V_{g,\mathrm{rms}}\bar{I}_{o,\mathrm{rms}}\sin^2\left(\omega_gt\right) \tag{15}$$

where V_{in}, I_{in}, I_{pri}, V_g, and $\bar{I}_o$ are, respectively, the average values of the input voltage, the input current, the primary-side current of the transformer, and the output current over a switching cycle; $V_{g,\mathrm{rms}}$ and $\bar{I}_{o,\mathrm{rms}}$ are, respectively, the rms values of the grid voltage and the output current; P_o is the output power; and ω_g is the grid angular frequency.

When S_1 is turned ON, i_{pri} increases and its energy is stored in the magnetizing inductance L_m while transferred into the secondary-side of the transformer. I_{pri} can be represented as

$$I_{\mathrm{pri}}=\frac{1}{T_s}\int_0^{d_1T_s}\left(i_{L_m}+ni_{\mathrm{sec}}\right)dt=\frac{V_{\mathrm{in}}{d_1}^2T_s}{2L_{eq}} \tag{16}$$

where $L_{eq}=L_mL_1/(n^2L_m+L_1)$.

$$\dot{\mathbf{x}}(t)=\begin{bmatrix}0 & -\left(\frac{d_2(t)}{nL_m}+nM_1(t)\right) & n\left(r_{L_1}+r_{C_2}\right)M_1(t) & nM_1(t) & -nM_1(t)r_{C_2}\\ \frac{1-d_1(t)}{nC_1} & 0 & -\frac{d_1(t)}{C_1} & 0 & 0\\ 0 & M_1(t)+\frac{d_1(t)}{L_1} & -\left(r_{L_1}+r_{C_2}\right)\left(M_1(t)+M_2(t)\right) & -\left(M_1(t)+M_2(t)\right) & r_{C_2}\left(M_1(t)+M_2(t)\right)\\ 0 & 0 & \frac{1}{C_2} & 0 & -\frac{1}{C_2}\\ 0 & 0 & \frac{r_{C_2}}{L_f} & \frac{1}{L_f} & -\frac{r_{L_f}+r_{C_2}}{L_f}\end{bmatrix}$$

$$\cdot\mathbf{x}(t)+\begin{bmatrix}\frac{d_1(t)}{L_m} & 0\\ 0 & 0\\ \frac{nd_1(t)}{L_1} & 0\\ 0 & 0\\ 0 & -\frac{1}{L_f}\end{bmatrix}\cdot\begin{bmatrix}v_{\mathrm{in}}(t)\\ v_g(t)\end{bmatrix} \tag{1}$$

$$y(t)=\begin{bmatrix}0 & 0 & 0 & 0 & 1\end{bmatrix}\mathbf{x}(t) \tag{2}$$

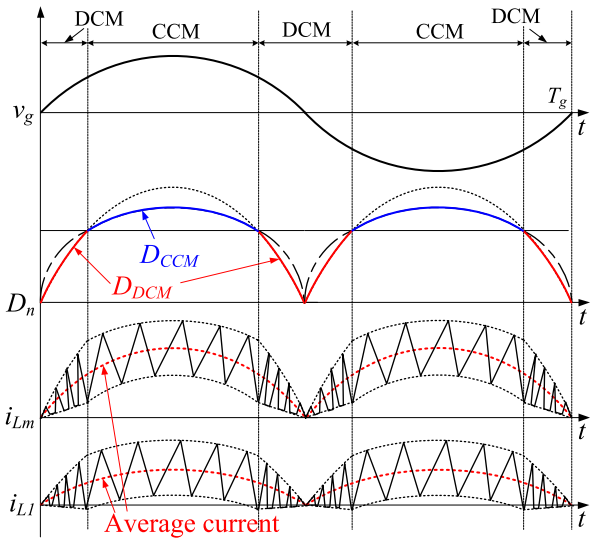

Fig. 4. Waveforms of the proposed bridgeless Zeta inverter operating in DCM and CCM during a grid period.

Substituting (16) into (15), we have the nominal duty ratio during DCM

$$D_{\text{DCM}}(t) = \frac{2}{V_{\text{in}}}\sqrt{\frac{L_{eq}P_o}{T_s}}|\sin(\omega_g t)|. \tag{17}$$

When the bridgeless Zeta inverter operates in CCM, the nominal duty-ratio can be derived using the voltage-second balance law. By neglecting the parasitic resistance values R_{L_1}, R_{L_f}, and R_{C_3} and by using the voltage-second balance for inductors L_m, L_1, and L_f over a switching period T_s, we can easily derive the nominal duty ratio during CCM

$$D_{\text{CCM}}(t) = \frac{|V_g|}{nV_{\text{in}} + |V_g|}. \tag{18}$$

C. Boundary of Operation Modes

The proposed bridgeless Zeta inverter operates in DCM at low instantaneous power level, then starts to operate in CCM as the instantaneous power level increases (see Fig. 4). The operating mode of the proposed inverter can be categorized into DCM and CCM by comparing the average inductor current and the halves of inductor current ripple (see Fig. 3). To simplify the problem of solving the inequality, the dc-offset current I_X is eliminated by comparing $\bar{I}_{L_m} + n|\bar{I}_{L_1}|$ and $\frac{1}{2}(\triangle i_{L_m} + n\triangle i_{L_1})$. Here, $\bar{I}_{L_m}$ is the average current flowing through L_m over a switching cycle and $\bar{I}_{L_1}$ is the average current flowing through L_1 over a switching cycle. If $\bar{I}_{L_m} + n|\bar{I}_{L_1}| \le \frac{1}{2}(\triangle i_{L_m} + n\triangle i_{L_1})$, the bridgeless Zeta inverter operates in DCM; otherwise it operates in CCM.

By applying the current-second balance law to the capacitor C_1 in CCM, the relationship between average currents $\bar{I}_{L_m}$ and $\bar{I}_{L_1}$ can be expressed as

$$\frac{\bar{I}_{L_m}}{nD_{\text{CCM}}(t)} = \frac{|\bar{I}_{L_1}|}{1 - D_{\text{CCM}}(t)}. \tag{19}$$

From (9) and (10)

$$\triangle i_{L_m} + n\triangle i_{L_1} = \frac{V_{\text{in}}T_s}{L_{eq}}D_{\text{CCM}}(t). \tag{20}$$

If the currents flowing through L_m and L_1 satisfy

$$\bar{I}_{L_m} + n|\bar{I}_{L_1}| \ge \frac{1}{2}(\triangle i_{L_m} + n\triangle i_{L_1}). \tag{21}$$

Then, it operates in CCM; otherwise, it operates in DCM. Substituting (19) and (20) into (21) yields

$$\frac{n|\bar{I}_{L_1}|}{1 - D_{\text{CCM}}(t)} \ge \frac{V_{\text{in}}T_s}{2L_{eq}}D_{\text{CCM}}(t). \tag{22}$$

Substituting (18) into the left-hand side of (22) and rearranging it yields

$$\sqrt{\frac{2L_{eq}|V_g||\bar{I}_{L_1}|}{V_{\text{in}}^2 T_s}} \ge D_{\text{CCM}}(t). \tag{23}$$

By the current-second balance law to C_2, $\bar{I}_{L_1} = \bar{I}_o$. Then, using $|V_g||\bar{I}_o| = 2P_o\sin^2(\omega_g t)$, (23) becomes

$$\frac{2}{V_{\text{in}}}\sqrt{\frac{L_{eq}P_o}{T_s}}|\sin(\omega_g t)| = D_{\text{DCM}}(t) \ge D_{\text{CCM}}(t). \tag{24}$$

Then, if $D_{\text{DCM}}(t) \ge D_{\text{CCM}}(t)$, the bridgeless Zeta inverter operates in CCM; otherwise it operates in DCM. In addition, the critical duty ratio D_{crit} can be obtained when $D_{\text{DCM}}(t) = D_{\text{CCM}}(t)$. Substituting the derived nominal duty ratio values (17) and (18) into $D_{\text{DCM}}(t) = D_{\text{CCM}}(t)$ and rearranging it yield

$$D_{\text{crit}} = 1 - \frac{n}{V_{g,\text{rms}}}\sqrt{\frac{2L_{eq}P_o}{T_s}}. \tag{25}$$

D. Optimal Boundary for Minimal Loss

A bridgeless Ćuk inverter in [22] mainly uses an input inductor, an output inductor, and buffer capacitors at primary/secondary sides in its power transfer. The transformer is assumed to be ideal and so its design is straightforward. However, the proposed bridgeless Zeta inverter uses the magnetizing inductance, the output inductor, and the buffer capacitor at secondary side in the power transfer. Thus, the transformer design becomes complicated. In this section, we provide the parameter selection of the transformer in detail.

Transformer turns ratio n and inductances L_m and L_1 mainly affect the switching and conduction losses in switches $S_1 - S_5$, and the core and copper losses in transformer T and inductor L_1 in the bridgeless Zeta inverter. These losses take a large portion of the overall power conversion losses, so parameters n, L_m, and L_1 should be carefully selected. The losses during the grid period can be represented as

$$\begin{aligned}\bar{P}_{\text{loss}}&(N_p, N_s, L_m, L_1)\\ &= \frac{1}{T_g}\int_0^{T_g}[P_S(i_o(t), v_g(t), n, L_m, L_1) + P_L(i_o(t), v_g(t), n, L_1)\\ &\quad + P_T(i_o(t), v_g(t), N_p, N_s, L_m, L_1)]\,dt\end{aligned} \tag{26}$$

TABLE I
VOLTAGE AND CURRENT STRESSES ON ACTIVE SWITCHING DEVICES

$v_g > 0$	$v_g < 0$	Phase	Mode	Voltage / Current	Values
S_1		I	DCM	Peak current	$v_{in}T_s d_1\left(\frac{1}{L_m}+\frac{n^2}{L_1}\right)$
			CCM	Peak current	$\frac{\lvert i_o\rvert}{v_{in}}\left(\lvert v_g\rvert + nv_{in}\right)+\frac{v_{in}T_s d_1}{2}\left(\frac{1}{L_m}+\frac{n^2}{L_1}\right)$
		II	Both	Voltage	$v_{in}+\frac{\lvert v_g\rvert}{n}$
		III	DCM	Voltage	v_{in}
S_3, S_4	S_2, S_5	I	DCM	Peak current	$-\frac{I_X}{n}+\frac{nv_{in}d_1T_s}{L_1}$
			CCM	Peak current	$\lvert i_o\rvert+\frac{nv_{in}d_1T_s}{2L_1}$
		II	DCM	Peak current	$\frac{v_{in}d_1T_s}{2}\left(\frac{1}{nL_m}+\frac{n}{L_1}\right)$
			CCM	Peak current	$\frac{\lvert i_o\rvert}{2v_{in}}\left(\frac{\lvert v_g\rvert}{n}+v_{in}\right)+\frac{v_{in}d_1T_s}{4}\left(\frac{1}{nL_m}+\frac{n}{L_1}\right)$
		III	DCM	Peak current	$-\frac{I_X}{n}$
S_2 & S_5	S_3 & S_4	I	Both	Voltage	$nv_{in}+\lvert v_g\rvert$
		II	DCM	Peak current	$\frac{v_{in}d_1T_s}{2}\left(\frac{1}{nL_m}+\frac{n}{L_1}\right)$
			CCM	Peak current	$\frac{\lvert i_o\rvert}{2v_{in}}\left(\frac{\lvert v_g\rvert}{n}+v_{in}\right)+\frac{v_{in}d_1T_s}{4}\left(\frac{1}{nL_m}+\frac{n}{L_1}\right)$
		III	DCM	Voltage	$\lvert v_g\rvert$

where the loss caused by switches is $P_S=\sum_{i=1}^{5}(P_{S\_\text{cond}}^{(i)}+P_{S\_\text{sw}}^{(i)})$; $P_{S\_\text{cond}}^{(i)}$ and $P_{S\_\text{sw}}^{(i)}$ are, respectively, the conduction and switching losses of S_i for $i=1,...,5$; the loss caused by inductor L_1 is $P_L=P_{L\_\text{core}}+P_{L\_\text{copper}}$ where P_{L_core} and P_{L_copper} are, respectively, the core and copper losses of L_1; the loss caused by transformer T is $P_T=P_{T\_\text{core}}+P_{T\_\text{copper}}$ where P_{T_core} and P_{T_copper} are, respectively, the core and copper losses of T. These losses can be calculated from the on-state currents and off-state voltages (see Table I) and parameters of the components (see Table II); the calculation method has been addressed in detail [23], [24] and so is omitted for brevity.

However, $\bar{P}_{\text{loss}}$ in (26) is a function of four parameters N_p, N_s, L_m, and L_1. Optimization of the four parameters that minimize the power loss is a complex computational task. Thus, we first set two parameters: magnetizing inductance $L_m=60.2\ \mu$H and primary turns of transformer $N_p=14$. Then, $\bar{P}_{\text{loss}}$ becomes a function of only two parameters: n and L_1 (see Fig. 5). When $3.4<n<3.7$ and $L_1>2$ mH, $\bar{P}_{\text{loss}}$ remains very small. Increase in inductance L_1 also increases the size of the inductor, so we set n and L_1 to be $n=3.64$ and $L_1=2.04$ mH in the prototype implementation.

From (25), the critical duty ratio depends on the value of $L_{eq}=L_mL_1/(n^2L_m+L_1)$ (see Fig. 6). With the obtained optimal values of L_m, L_1, and n, the resulting critical duty ratio can be calculated as $D_{\text{crit}}=0.29$, which balances the operating regions between DCM and CCM; the DCM region is 20.9% of a grid period and CCM region is 79.1%.

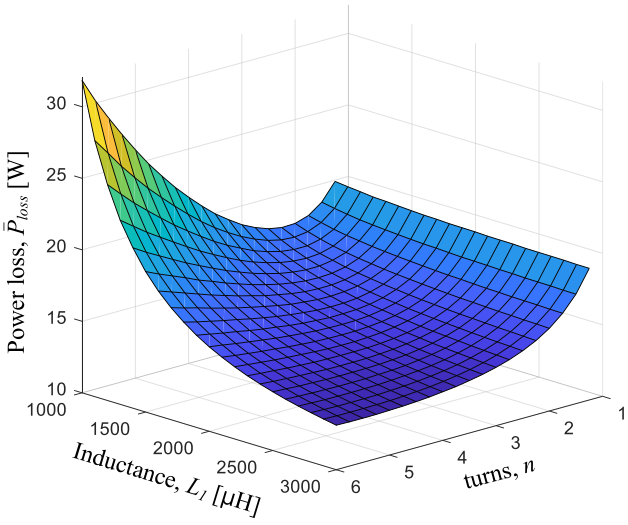

Fig. 5. Losses in (26) during a grid period with respect to turns ratio n and inductance L_1.

IV. CONTROL DESIGN

The control system of the bridgeless hybrid-mode Zeta inverter aims at making its output current track the reference current, which is synchronized with the grid voltage. To stabilize the hybrid-mode Zeta inverter, a conventional PI controller can be applied for each mode. The transfer functions of PI controllers in DCM and CCM are represented as

$$C_{\text{PI}\_\rho}(z)=k_{p\_\rho}+k_{i\_\rho}\frac{T_s}{2}\frac{1+z^{-1}}{1-z^{-1}},\ \text{for } \rho=\text{DCM or CCM} \tag{27}$$

where k_{p_ρ} and k_{i_ρ} are, respectively, the proportional and integral controller gains for $\rho=$ DCM or CCM.

TABLE II
PARAMETERS AND COMPONENTS OF THE BRIDGELESS ZETA-BASED INVERTER

Parameter	Value	Parameter	Value
Input voltage	40-50 V	Grid frequency	60 Hz
Grid voltage	220 V_{rms}	Switching frequency	50 kHz
Rated power	300 W	Sampling frequency	50 kHz

Component	Part number	Detail
Primary-side switch	IPP120N20NFD	V_{ds} = 200 V $R_{ds.on}$ = 12 mΩ
Secondary-side switches	UJ3C120070K3S	V_{ds} = 1200 V $R_{ds.on}$ = 70 mΩ
Input capacitor	SAMWHA HK 450 V	C_{in} = 810 uF
First capacitor	PHE840M	C_1 = 470 nF
Second capacitor	PHE840M	C_2 = 470 nF
First inductance	CH400125G	L_1 = 2.04 mH
Filter inductance	CH270125G	L_f = 356 μH
Current Sensor	L18P010D15	V_{cc} = ±15 V $I_{cc} \leq$ 15 mA
Voltage Sensor	LM358	V_{cc} = 5 V $I_{cc} \leq$ 2 mA
Gate Driver	SI8275GB-IS1	V_i = 5 V V_d = 15 V

Transformer property	Value
Transformer size (Length/Width/Height)	PQ3535 (35.5/39.1/37.6 mm)
Core shape	0T43535UG, *Magnetics* (A_e=190.0 mm^2, V_e=16.3 cm^2)
Core material	Ferrite T material, *Magnetics* (μ_i=3000, B_{sat}=530 mT)
Turns ratio, n	3.64
Primary winding, N_p	14 turns, 16AWG x 2
Secondary winding, N_s	51 turns, 16AWG
Magnetic inductance	60.2 μH
Primary-side leakage inductance	0.37 μH

However, the conventional PI controller cannot meet the desired control precision due to the different system dynamics in the hybrid-mode Zeta inverter and the grid disturbance. Especially, the system dynamics of the bridgeless Zeta inverter that operates in CCM has RHP zeros, which generate phase-lags and limit the increase of the PI controller gains. In addition, this circuit undergoes the severe grid disturbance when connected to the utility grid. To solve these problems, we propose to use an RC with a phase-lead compensator for each mode. To alleviate the control burden from the feedback controller, nominal duty ratios are also derived for a feedforward control input. This section will

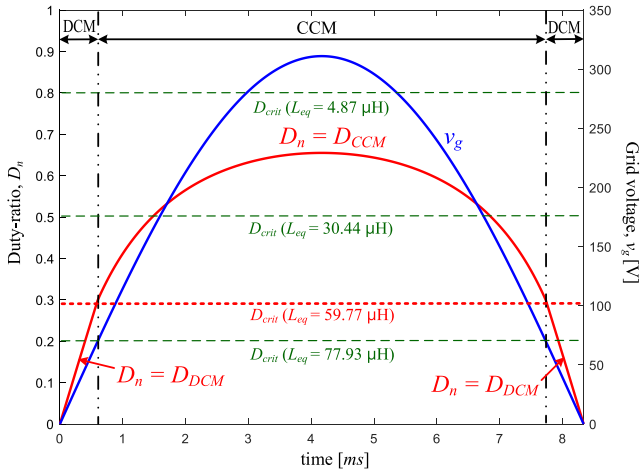

Fig. 6. Operating regions and critical duty ratios with different values of L_{eq}.

first introduce nominal duty ratio values as a feedforward input and develop an RC that has a multiple phase-lead compensator.

A. Feedforward Controller

The nominal duty ratio D_n for the hybrid-mode Zeta inverter is

$$D_n(t) = \begin{cases} D_{\text{DCM}}(t), & \text{if } D_{\text{DCM}}(t) < D_{\text{CCM}}(t) \\ D_{\text{CCM}}(t), & \text{if } D_{\text{DCM}}(t) \geq D_{\text{CCM}}(t). \end{cases} \tag{28}$$

These nominal duty ratios in DCM and CCM were obtained as in Section III-B. Although the nominal duty ratio D_n does not directly generate the desired output current, the use of D_n assists the proposed inverter to produce the desired output current while lowering the burden of the feedback controller.

B. RC With Multiple Phase-Lead Compensator

The RC is an effective approach to track a periodic reference signal and to reject the disturbance at specified frequencies [25]–[28]. However, if the hybrid-mode Zeta inverter adopts the RC by itself, the different phase lag incurred by the different system dynamics in DCM and CCM may severely deteriorate the control accuracy of the RC. Thus, the proposed RC adopts a multiple phase-lead compensator to compensate for the incurred phase lag of the hybrid-mode Zeta inverter.

The proposed RC for the hybrid-mode Zeta inverter is described as

$$C_{\text{RC\_}\rho}(z) = k_{r\_\rho} \frac{z^{-N} Q_\rho(z)}{1 - z^{-N} Q_\rho(z)} G_{\text{pl\_}\rho}(z) \tag{29}$$

where k_{r_ρ} and $Q_\rho(z)$ are, respectively, the RC gain and the LPF for ρ = DCM or CCM; $N = f_s/f_g$ where $f_s = 1/T_s$ and f_g are, respectively, the switching and reference frequencies; and $G_{\text{pl\_}\rho}(z)$ is the phase-lead compensator to compensate for the phase lag of the closed-loop systems for ρ = DCM or CCM. Because of disturbances and parameter uncertainties, the inverse of the plant to implement the phase-lead compensator is often unrealizable, so a linear phase-lead compensator [27]–[29] is

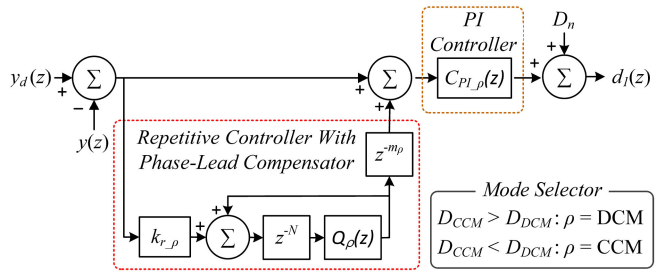

Fig. 7. Block diagram of control system for the hybrid-mode Zeta inverter. $y(z)$ and $y_d(z)$ are, respectively, the output and the reference output trajectory.

chosen as follows:

$$G_{\text{pl\_}\rho}(z) = z^{m_\rho} \tag{30}$$

where m_ρ is the integer phase-lead step for $\rho =$ DCM or CCM.

The whole control system (see Fig. 7) comprises a PI controller term that drives the closed-loop system to stay within a uniform bound, a hybrid-mode nominal duty ratio term that eases the feedback control burden, and an RC that has a multiple phase-lead compensator term that substantially increases the tracking accuracy.

To analyze the stability of the proposed control system (see Fig. 7), the small-signal models (see Section II) are represented as $G_{id\_\rho}(z)$ for $\rho =$ DCM or CCM. By obtaining the sensitivity function of the closed-loop system and by applying the small-gain theorem to its modified function, the stability analysis of the modified control system gives the sufficient stability conditions [27]–[29], which are as follows.

1) The closed-loop system $G_{\text{cl\_}\rho}(z)$ is stable.
2) $|Q_\rho(z)| \le 1$, for all $z = e^{j\omega T_s}$, where $0 < \omega < \frac{\pi}{T_s}$, and its cutoff frequency is ω_{c_ρ}.
3) $|1 - k_{r\_\rho} z^{m_\rho} G_{pi\_\rho}(z) G_{p\_\rho}(z)(1 - G_{\text{cl\_}\rho}(z))| < 1$, for all $z = e^{j\omega T_s}$, where $0 < \omega < \omega_{c\_\rho}$.

Here, $G_{\text{cl\_}\rho}(z)$ is the closed-loop transfer function without the RC

$$G_{\text{cl\_}\rho}(z) = \frac{G_{\text{PI\_}\rho}(z) G_{id\_\rho}(z)}{1 + G_{\text{PI\_}\rho}(z) G_{id\_\rho}(z)}. \tag{31}$$

C. Control Parameter Selection

Based on the system models in (7) and (8), the discrete-time transfer functions at the instantaneous peak power operating points in DCM and CCM are

$$G_{id\_\rho}(z) = \begin{cases} \frac{4.56z^4+5.08z^3-5.47z^2-4.45z-0.01}{z^5+0.06z^4-1.69z^3+0.13z^2+0.96z} & \text{with } \rho = \text{DCM} \\ \frac{3.73z^4-0.67z^3-7.79z^2+3.74z+4.31}{z^5-0.84z^4-1.59z^3+1.69z^2+0.68z-0.94} & \text{with } \rho = \text{CCM}. \end{cases} \tag{32}$$

Based on the aforementioned transfer functions and system parameters (see Table II), this section will introduce a design process of the control parameters to meet the stability conditions (see Section IV-B).

1) Stability Condition (a): To satisfy stability condition (a), we should select the control parameters in $G_{\text{PI\_}\rho}(z)$ such that $G_{\text{cl\_}\rho}(z)$ does not have any poles outside the unit circle in the z-plane. Then, the PI controllers $G_{\text{pi\_}\rho}(z)$ with $\rho =$ DCM or CCM are designed with control parameters $k_{p\_}\rho = 0.01$ and $k_{i\_}\rho = 0.1$.

2) Stability Condition (b): The LPF $Q_\rho(z)$ is needed to improve the system robustness. To satisfy stability condition (b), $Q_\rho(z)$ is selected as a q-order LPF with zero-phase shift

$$Q_\rho(z) = \Sigma_{i=0}^{p} \alpha_i z^i + \Sigma_{i=1}^{p} \alpha_i z^{-i} \tag{33}$$

where $\alpha_0 + 2\Sigma_{i=1}^{p} \alpha_i = 1$ with $\alpha_i > 0$ and p is the number of samples used for filtering. Its cutoff frequency ω_{c_ρ} should be set high enough that harmonic components in a wide range of frequencies can be compensated, so ω_{c_ρ} will be set after the design of the phase-lead compensator in the RC.

For reduction of the computational burden, a first-order LPF is usually recommended in the RC design [11], [13], [14]. But, the first-order filter has limitation to lowering its cutoff frequency. To more decrease the cutoff frequency of $Q_\rho(z)$, a k-step first-order LPF is applied to guarantee the condition (b)

$$Q_\rho^{(k)}(z) = \alpha_0 z^0 + \frac{1}{2}\left(\alpha_1 z^k + \alpha_1 z^{-k}\right) \tag{34}$$

where $\alpha_0 + 2\alpha_1 = 1$ with $\alpha_i > 0$ and k is the sampling interval used for filtering. Then, by making its magnitude become -3 dB, its cutoff frequency can be obtained

$$\begin{aligned} |Q_\rho^{(k)}(e^{jm\omega_{c\_\rho}})| &= |\alpha_0 + \alpha_1\left(e^{jk\omega_{c\_\rho}T_s} + e^{-jk\omega_{c\_\rho}T_s}\right)| \\ &= |\alpha_0 + 2\alpha_1 \cos(m\omega_{c\_\rho}T_s)| = -3 \text{ dB} \end{aligned} \tag{35}$$

where $0 < \omega_{c\_\rho} < \pi/T_s$ and $\alpha_0 + 2\alpha_1 = 1$. Then

$$\omega_{c\_\rho} = \frac{1}{kT_s} \cos^{-1}\left(\frac{\frac{1}{\sqrt{2}} - \alpha_0}{1 - \alpha_0}\right) \tag{36}$$

where $\alpha_0 \ge 0.5$. The aforementioned equation indicates that sampling interval k can also adjust the cutoff frequency ω_{c_ρ} other than T_s and α_0.

3) Stability Condition (c): Based on the frequency-domain design tool [27]–[29], the closed-loop transfer function $G_{\text{cl\_}\rho}(z)$ and the phase-lead compensator z^{m_ρ} can be, respectively, rearranged into

$$G_{\text{cl\_}\rho}(e^{j\omega}) = N_{\text{cl\_}\rho}(e^{j\omega}) e^{j\theta_{\text{cl\_}\rho}(e^{j\omega})} \tag{37}$$

and

$$\theta_{m_\rho}(e^{j\omega}) = \angle z^{m_\rho}. \tag{38}$$

Then, simplifying inequality in stability condition (c) yields

$$|1 - k_{r\_\rho} N_{\text{cl\_}\rho}(e^{j\omega}) e^{j\left(\theta_{\text{cl\_}\rho}(e^{j\omega}) + \theta_{m_\rho}(e^{j\omega})\right)}| < 1 \tag{39}$$

where $0 < \omega < \omega_{c\_\rho}$.

Substituting $e^{j\theta} = \cos(\theta) + j\sin(\theta)$ and $k_{r\_\rho} > 0$ into (39) yields the sufficient conditions [27]–[29]

$$0 < k_{r\_\rho} < k_{r\_\rho\_\max} \triangleq \frac{2\cos(\theta_{\text{cl\_}\rho}(e^{j\omega}) + \theta_{m_\rho}(e^{j\omega}))}{N_{\text{cl\_}\rho}(e^{j\omega})} \tag{40}$$

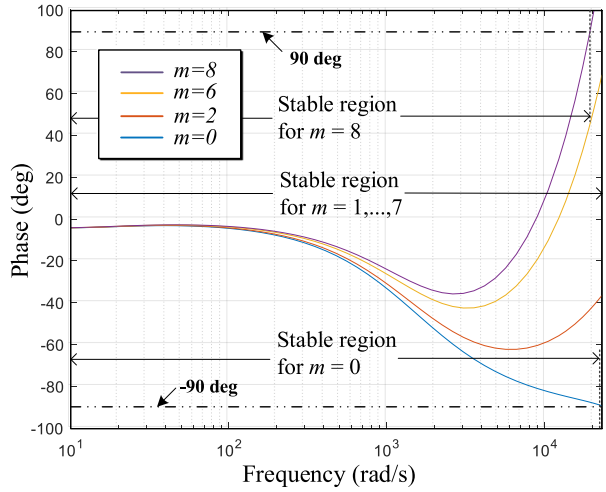

(a)

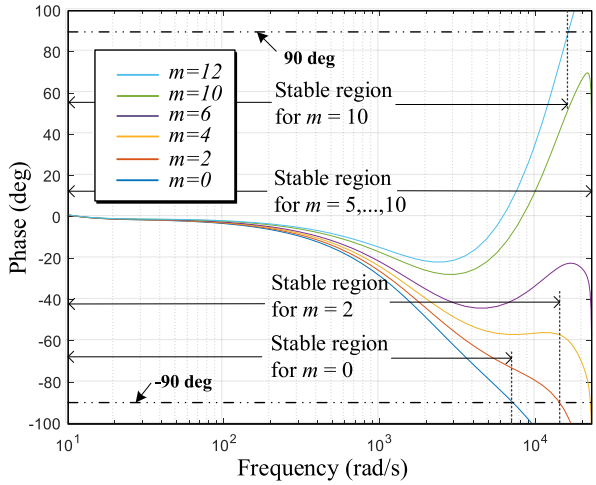

(b)

Fig. 8. Phase plots of $G_{\text{cl\_}\rho}z^{m_\rho}$ with (a) $\rho =$ DCM and (b) $\rho =$ CCM.

and

$$|\theta_{cl\_\rho}(e^{j\omega}) + \theta_{m_\rho}(e^{j\omega})| < \pi/2 \tag{41}$$

where $0 < \omega < \omega_{c\_\rho}$.

A phase-lead step m_ρ should be selected appropriately such that the angle in (41) is $\leq \pi/2$ at frequency $\leq \omega_{c\_\rho}$, so a phase-lead step m_ρ is chosen to maximize the frequency range to meet the inequality in (41), and the cutoff frequency ω_{c_ρ} is determined to be less than the crossover frequency at which $|\theta_{\text{cl}\_\rho}(e^{j\omega}) + \theta_{m_\rho}(e^{j\omega})| = \pi/2$.

The phase plots of $G_{\text{cl}\_\rho}(z)z^{m_\rho}$ (see Fig. 8) indicate that the closed-loop systems without phase-lead compensation do not guarantee condition (41) in a wide frequency range. The phase-lead compensation step values of $m_{\text{DCM}} = 1,...,7$ achieve the maximized stable frequency range with $\rho =$ DCM, whereas the phase-lead compensation step values of $m_{\text{CCM}} = 5,...,10$ does with $\rho =$ CCM. Considering unknown uncertainties and stability conditions in all DCM and CCM regions, the phase-lead compensation step values are set to be $m_{\text{DCM}} = 2$ and $m_{\text{CCM}} = 6$, respectively. Furthermore, if the cutoff frequency ω_{c_ρ} of the LPF is set as $\omega_{c\_\rho} = 20\,000$ rad/s, both of these compensators completely satisfy the condition (41). From (40), the ranges of RC gains that correspond to $m_{\text{DCM}} = 2$ and $m_{\text{CCM}} = 6$ are obtained as $0 < k_{r_{\text{DCM}}} < 1.93$ and $0 < k_{r_{\text{CCM}}} < 2.14$. The resulting RCs are

$$G_{\text{rc}\_\rho}(z) = \begin{cases} \dfrac{1}{4} \cdot \dfrac{z^{-N}Q_{\text{DCM}}(z)}{1 - z^{-N}Q_{\text{DCM}}(z)} z^2 & \text{with } \rho = \text{DCM} \\ \dfrac{1}{4} \cdot \dfrac{z^{-N}Q_{\text{CCM}}(z)}{1 - z^{-N}Q_{\text{CCM}}(z)} z^6 & \text{with } \rho = \text{CCM} \end{cases} \tag{42}$$

where $Q_\rho(z)$ is chosen as a three-step first-order LPF: $Q_\rho^{(3)}(z)$ is $0.225z^3 + 0.55 + 0.225z^{-3}$ with $\rho =$ DCM or CCM.

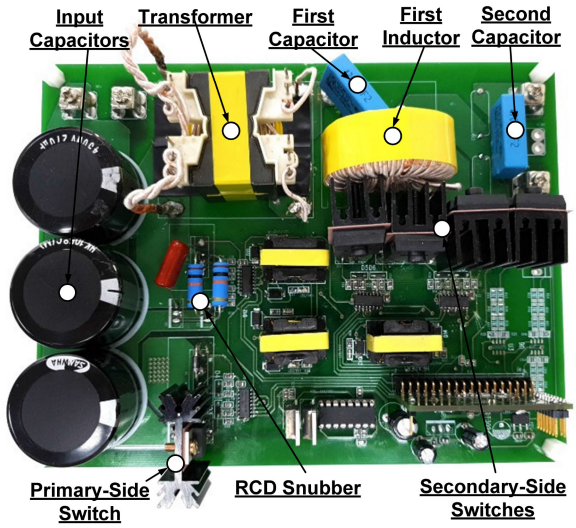

Fig. 9. Prototype of the proposed Zeta inverter.

V. Experimental Results and Discussion

A prototype of the bridgeless Zeta inverter is implemented to verify the theoretical analysis and evaluate its performance (see Fig. 9). Its input voltage range, grid voltage, and rated output power are set to be $v_{\text{in}} = 40 - 50$ V, $v_g = 220$ V_{rms}, and $P_o = 300$ W. Table II summarizes the specifications of the other major parameters and components in detail. A TMS320F28069 digital signal processor was used to implement the controller for the proposed inverter.

When only PI control scheme coupled with feedforward controller was used, the output current cannot track the reference output current accurately [see Fig. 10(a)]. When the RC without a phase lead compensator was used, the output current was distorted in both DCM and CCM due to the incorrect learning of the control input [see Fig. 10(b)]. When the RC with two-step phase lead was applied, the output current started to be distorted in CCM [see Fig. 10(c)]. However, when the proposed RC with two-step phase lead in DCM region and six-step phase lead in CCM region was used, the output current was almost sinusoidal and achieved desired power level at 300 W [see Fig. 10(d)].

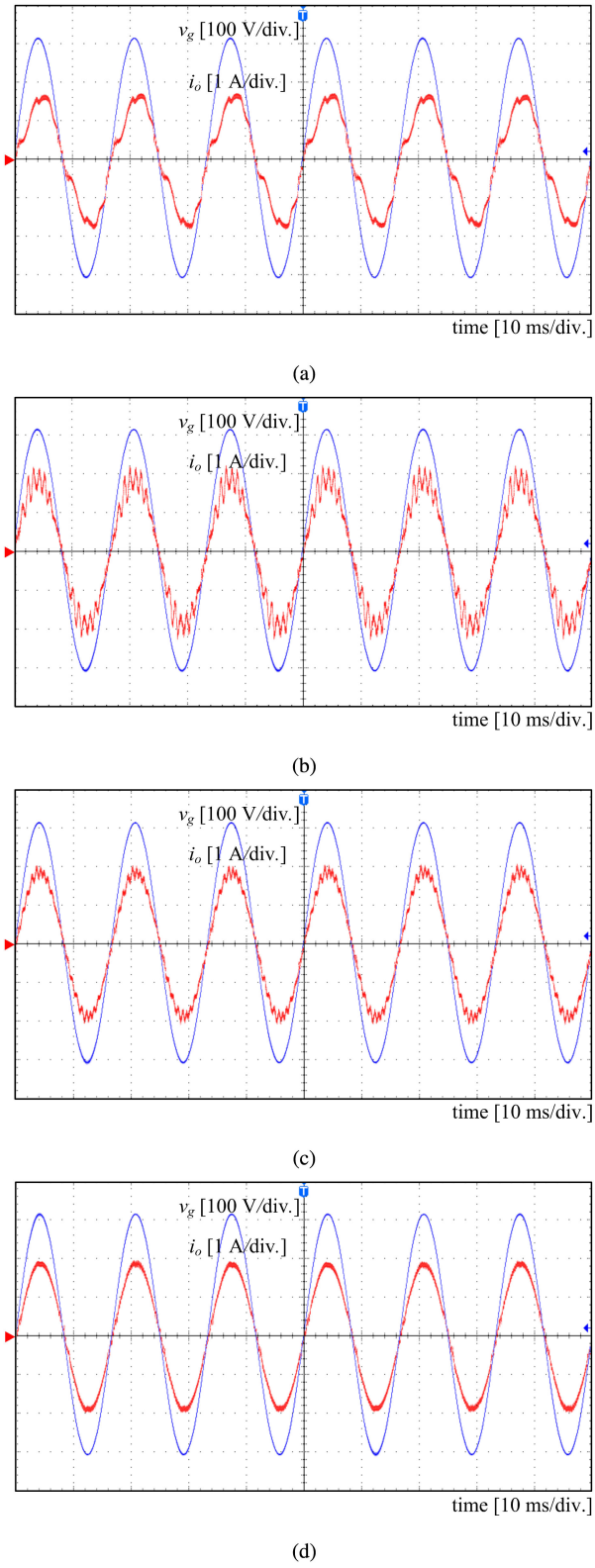

Fig. 10. Experimental waveforms of the grid voltage and output current at $v_{\text{in}} = 45$ V and $P_o = 300$ W. (a) No RC. (b) RC without phase-lead compensator. (c) RC with phase-lead step $m_{\text{DCM}} = 2$ and $m_{\text{CCM}} = 2$. (d) RC with phase-lead step $m_{\text{DCM}} = 2$ and $m_{\text{CCM}} = 6$.

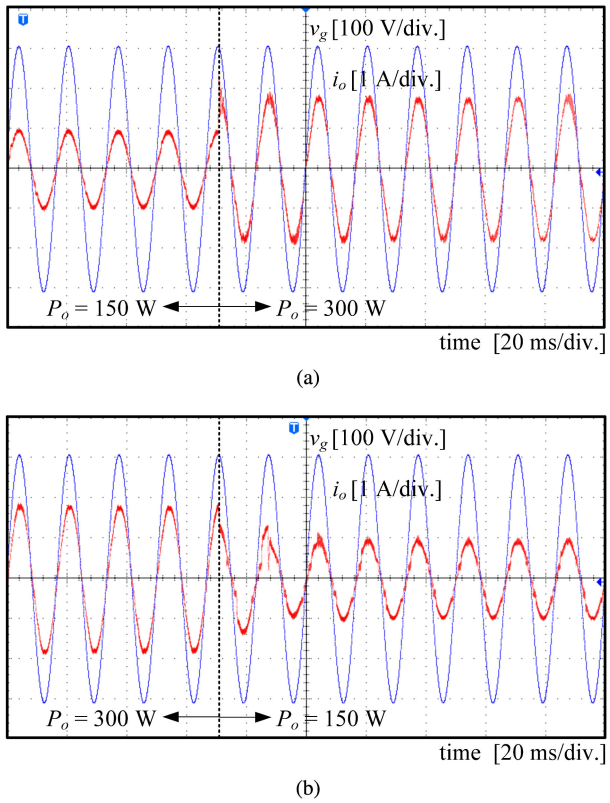

Fig. 11. Experimental waveforms of the grid voltage and output current at $v_{\text{in}} = 45$ V when the output power is varied with the proposed controller. (a) 150 to 300 W. (b) 300 to 150 W.

To validate the dynamic performance of the proposed Zeta inverter, the output power was varied from 150 to 300 W and vice versa. When the output power was changed, the output current well tracked the reference output current in a few iterations (see Fig. 11).

In Fig. 12(a), the voltage and current waveforms of S_1 were well matched with theoretical waveforms of S_1. Primary-side switch suffered from the voltage spike but it did not exceed the voltage rating of the primary-side switch. In Fig. 12(b), we have measured the voltage and current waveforms of S_4 and S_5 because the switch pairs (S_3, S_4) and (S_2, S_5) were turned ON and OFF simultaneously. The switch S_5 also suffered from the voltage spike but it did not exceed the voltage rating of S_5.

Fig. 13 shows the THD values of the output current for different load conditions. THD was measured less than 1.7% at the full load condition.

The power conversion efficiency was measured by Yokogawa WT1800E digital power analyzer. The maximum power conversion efficiency was 94.7% and the California Energy Commission weighted efficiency is 94.4% when $v_{\text{in}} = 50$ V (see Fig. 14). Fig. 15 shows the power loss distribution in the proposed Zeta inverter at full load. From Fig. 15, the primary-side switch takes 36.23% and the transformer takes 30.90% in total power loss.

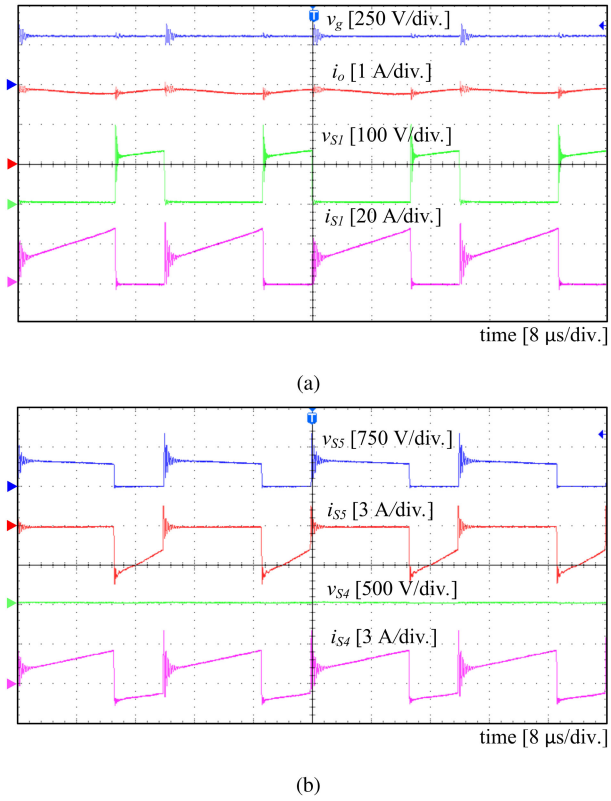

Fig. 12. Experimental waveforms of the drain-source voltage and drain current at $v_{\text{in}} = 45$ V and the instantaneous peak power. (a) In S_1. (b) In S_5 and S_4.

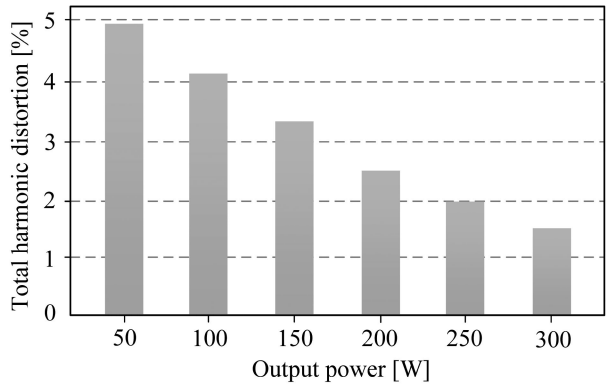

Fig. 13. THD of the output current at $v_{\text{in}} = 45$ V.

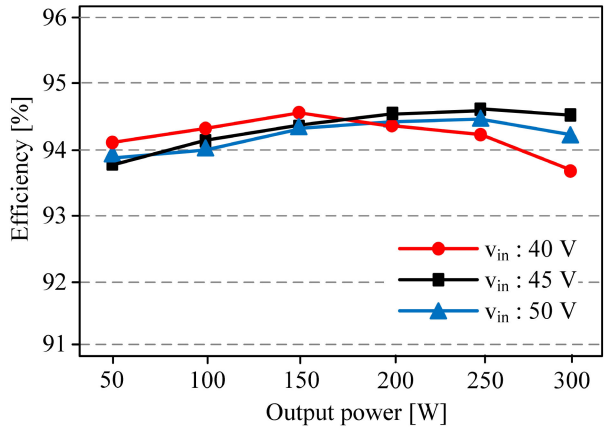

Fig. 14. Measured power conversion efficiency according to the output power and input voltage.

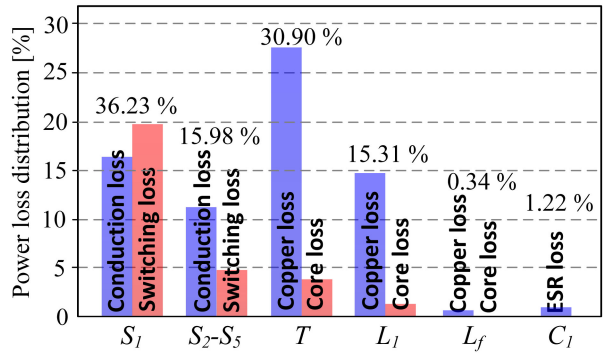

Fig. 15. Power loss distribution at $v_{\text{in}} = 45$ V and full load.

As in Table III, an unfolding-type flyback inverter in [13] features simple structure, low component number, and high efficiency. However, the primary-side switch and secondary-side diode suffer from high current ripple, which limits its power capacity. Compared to the unfolding-type flyback inverter, an unfolding-type Ćuk inverter in [27] has the advantages of low ripples of the current at the input and output, and medium power capacity. However, it requires a large number of passive power components, which increases the complexity of the power circuit design. The unfolding-type Zeta inverter in [16] features the inherent output inductor that generates the output current with low ripple; this inductor further reduces the ripple of the current that flows through the secondary-side diode compared to the unfolding-type flyback inverter. The inverter in [16] also uses smaller number of power components than those used in the unfolding-type Ćuk inverter. However, these unfolding-type inverters must use the unfolding bridge at the grid side. This bridge incurs a localized heat management problem. Also, the diode on the secondary side of the transformer conducts over one cycle of grid voltage, and this trait complicates the task of heat management. The structure of single-stage Zeta inverter in [21] can alleviate the localized heat management problem, but only one of the body diodes in the secondary-side switches conducts depending on the polarity of the grid voltage over one cycle of the grid voltage, so heat management is still a problem. On the other hand, in the proposed bridgeless Zeta inverter, the loss accumulated at the original secondary-side diode is distributed to all body diodes of the secondary-side switches. By means of balanced loss distribution, the proposed inverter achieves easy heat management and increased reliability. Moreover, it does not require the additional diode on the secondary side of the transformer or center-tapped transformer; this aspect simplifies the circuit structure and reduces the development cost of the circuit. The efficiency of the proposed bridgeless Zeta inverter is lower than or equal to that of the unfolding-type inverters, because the body diode of the secondary-side switch has a larger

TABLE III
COMPARISON OF UNFOLDING-TYPE FLYBACK/ĆUK INVERTERS AND ZETA TOPOLOGY BASED INVERTERS IN TERMS OF HARDWARE IMPLEMENTATION AND PERFORMANCE

		Unfolding flyback inverter	Unfolding Ćuk inverter	Zeta topology based inverters		
				Unfolding type	Single-stage type	Bridgeless type
Reference		[13]	[27]	[16]	[21]	This paper
# of components	S	5	5	5	5	5
	D	1	1	1	0	0
	L	0	2	1	1	1
	C	1	3	2	2	2
	T	1	1	1	1 (Center-tap)	1
# of high-frequency switching components		2 (S_1, D_1)	2 (S_1, D_1)	2 (S_1, D_1)	2 (S_1, D_{S3} or D_{S5})	3 (S_1, $D_{S2,5}$ or $D_{S3,4}$)
Value of components	L	$L_f = 400$ μH	$L_1 = 360$ μH $L_2 = 680$ μH $L_f = 210$ μH	$L_1 = 22$ mH $L_f = 100$ μH	$L_1 = 5$ mH $L_f = 100$ μH	$L_1 = 2.04$ mH $L_f = 356$ μH
	C	$C_1 = 1$ μF	$C_1 = 4.4$ μF $C_2 = 100$ nF $C_3 = 100$ nF	$C_1 = 680$ nF $C_2 = 1$ μF	$C_1 = 640$ nF $C_2 = 1$ μF	$C_1 = 470$ nF $C_2 = 470$ nF
	n	1:3.64	1:2.82	1:3.64	1:6:6	1:3.64
Switching frequency	f_s	50 kHz	40 kHz	20 kHz	100 kHz	50 kHz
Voltage stress[1)] of switch		S_1: 0.43 p.u, D_1: 1.50 p.u, $S_{2,5}$(or $S_{3,4}$) : 1.0 p.u	S_1: 0.58 p.u, D_1: 1.52 p.u, $S_{2,5}$(or $S_{3,4}$) : 1.0 p.u	S_1: 0.42 p.u, D_1: 1.48 p.u, $S_{2,5}$(or $S_{3,4}$) : 1.0 p.u	S_1: 0.32 p.u, S_3(or S_4) : 1.88 p.u, S_5(or S_2) : 1.88 p.u	S_1: 0.42 p.u, $S_{2,5}$(or $S_{3,4}$) : 1.48 p.u
Current stress[1)] of switch		S_1: 10.8 p.u, D_1: 2.84 p.u, $S_{2,5}$(or $S_{3,4}$) : 1.0 p.u	S_1: 10.3 p.u, D_1: 2.91 p.u, $S_{2,5}$(or $S_{3,4}$) : 1.0 p.u	S_1: 10.3 p.u, D_1: 2.83 p.u, $S_{2,5}$(or $S_{3,4}$) : 1.0 p.u	S_1: 13.2 p.u, S_2(or S_5), : 1.3 p.u, S_3(or S_4) : 2.08 p.u S_4(or S_3) : 1.0 p.u	S_1 10.8 p.u, $S_{2,5}$(or $S_{3,4}$) : 1.41 p.u, $S_{3,4}$(or $S_{2,5}$) : 1.0 p.u
Efficiency		96.73 %	95.75 %	96.80 %	95.11 %	95.76 %

#, S, D, L, C, and T stand for number, switch, diode, inductor, capacitor, and transformer, respectively.
[1)] Benchmark value—Switch voltage and current stresses, $v_g = 1.0$ p.u., $i_o = 1.0$ p.u. at the instantaneous peak power with full load $P_o = 300$ W; component parameters in other topologies were designed based on their own references.

voltage drop compared to that of the diode itself. This can be reduced if the proposed inverter adopts the secondary-side switches having a lower voltage drop at their body diodes. Also, the efficiency of proposed inverter is higher than the single-stage Zeta inverter in [21], because its transformer turns ratio used in [21] was set to be high.

VI. CONCLUSION

This article introduces a bridgeless Zeta inverter and presents its dynamic models and control methods. By means of bridgeless structure and balanced loss distribution characteristic, the proposed inverter features reduced number of power components, compact size, and high reliability. Moreover, we have designed the proposed inverter to operate in DCM and CCM. We first identified the mode boundaries and investigated the dynamic characteristic of the proposed inverter for each mode. We derived the transfer function corresponding to each operation mode and used it to design the nominal duty ratio as well as the feedback controller. To compensate for different periodic disturbances and phase lags incurred by the different system dynamics in DCM and CCM, we implemented different RCs with different phase-lead compensation algorithms in the proposed control scheme. We also provided detailed and practical design guidelines to design a stable hybrid-mode Zeta inverter. To confirm the validity of the proposed inverter, we have built a 300-W prototype inverter and used it for experimental tests.

APPENDIX A

The average model (1) can be described by the nonlinear differential equation $\dot{\mathbf{x}}(t) = \mathbf{F}(\mathbf{x}(t), d_1(t))$, where

$\mathbf{F} = [F_1, F_2, F_3, F_4]^T$ is a nonlinear functions and $\mathbf{x} = [x_1, x_2, x_3, x_4]^T$ is the state vector. Linearizing (1) yields the small-signal model in (3). The parameters used in (3) are provided as (43)–(52), as shown at the bottom of this page, where

$$\frac{\partial M_1}{\partial \hat{x}_1} = -\frac{2L_{eq}}{D_1 T_s V_{\text{in}} L_{1m}} \tag{53}$$

$$\frac{\partial M_1}{\partial \hat{x}_2} = \frac{2n\left(I_{L_m} + nI_{L_1}\right) L_m L_{eq}}{D_1 T_s V_{\text{in}}^2 L_{1m}^2} \tag{54}$$

$$\frac{\partial M_1}{\partial \hat{x}_3} = -\frac{2nL_{eq}}{D_1 T_s V_{\text{in}} L_{1m}} \tag{55}$$

$$\frac{\partial M_1}{\partial \hat{x}_4} = -\frac{2n\left(I_{L_m} + nI_{L_1}\right) L_m L_{eq}}{D_1 T_s V_{\text{in}}^2 L_{1m}^2} \tag{56}$$

$$\frac{\partial M_1}{\partial \hat{d}_1} = \frac{2\left(I_{L_m} + nI_{L_1}\right) L_{eq}}{D_1^2 T_s V_{\text{in}} L_{1m}}. \tag{57}$$

APPENDIX B

The system parameters as defined in (7) and (8) are given as (58)–(77), as shown at the bottom of this page and the next page.

$$\frac{\partial F_1}{\partial \hat{x}_1} = \frac{\partial M_1}{\partial \hat{x}_1}\left(\frac{V_{C_1}}{nL_{1m}L_m} - nV_{C_1} + n\left(r_{L_1} + r_{C_2}\right) I_{L_1} + nV_{C_2} - nr_{C_2} I_o\right) \tag{43}$$

$$\frac{\partial F_1}{\partial \hat{x}_2} = -\frac{D_2}{nL_m} - n\bar{M}_1 + \frac{\partial M_1}{\partial \hat{x}_2}\left(\frac{L_1 V_{C_1}}{nL_{eq}} - nV_{C_1} + n\left(r_{L_1} + r_{C_2}\right) I_{L_1} + nV_{C_2} - nr_{C_2} I_o\right) \tag{44}$$

$$\frac{\partial F_1}{\partial \hat{x}_3} = n\bar{M}_1\left(r_{L_1} + r_{C_2}\right) + \frac{\partial M_1}{\partial \hat{x}_3}\left(\frac{V_{C_1}}{nL_{1m}L_m} - nV_{C_1} + n\left(r_{L_1} + r_{C_2}\right) I_{L_1} + nV_{C_2} - nr_{C_2} I_o\right) \tag{45}$$

$$\frac{\partial F_1}{\partial \hat{x}_4} = n\bar{M}_1 + \frac{\partial M_1}{\partial \hat{x}_4}\left(\frac{L_1 V_{C_1}}{nL_{eq}} - nV_{C_1} + n\left(r_{L_1} + r_{C_2}\right) I_{L_1} + nV_{C_2} - nr_{C_2} I_o\right) \tag{46}$$

$$\frac{\partial F_1}{\partial \hat{d}_1} = \frac{V_{C_1}}{nL_m} + \frac{V_{\text{in}}}{L_m} + \frac{\partial M_1}{\partial d_1}\left(\frac{L_{1m} V_{C_1}}{nL_m} - nV_{C_1} + n\left(r_{L_1} + r_{C_2}\right) I_{L_1} + nV_{C_2} - nr_{C_2} I_o\right) \tag{47}$$

$$\frac{\partial F_3}{\partial \hat{x}_1} = \frac{\partial M_1}{\partial \hat{x}_1}\left(V_{C_1} + \frac{n^2 L_m}{L_1}\left(\left(r_{L_1} + r_{C_2}\right) I_{L_1} + V_{C_2} - r_{C_2} I_o\right)\right) \tag{48}$$

$$\frac{\partial F_3}{\partial \hat{x}_2} = \bar{M}_1 + \frac{D_1}{L_1} + \frac{\partial M_1}{\partial \hat{x}_2}\left(V_{C_1} + n^2 L_m^2 L_1 L_{1m}\left(\left(r_{L_1} + r_{C_2}\right) I_{L_1} + V_{C_2} - r_{C_2} I_o\right)\right) \tag{49}$$

$$\frac{\partial F_3}{\partial \hat{x}_3} = -\left(r_{L_1} + r_{C_2}\right)\left(\bar{M}_1 + \bar{M}_2\right) + \frac{\partial M_1}{\partial \hat{x}_3}\left(V_{C_1} + \frac{n^2 L_m}{L_1}\left(\left(r_{L_1} + r_{C_2}\right) I_{L_1} + V_{C_2} - r_{C_2} I_o\right)\right) \tag{50}$$

$$\frac{\partial F_3}{\partial \hat{x}_4} = -\left(\bar{M}_1 + \bar{M}_2\right) + \frac{\partial M_1}{\partial \hat{x}_4}\left(V_{C_1} + n^2 L_m^2 L_1 L_{1m}\left(\left(r_{L_1} + r_{C_2}\right) I_{L_1} + V_{C_2} - r_{C_2} I_o\right)\right) \tag{51}$$

$$\frac{\partial F_3}{\partial \hat{d}_1} = \frac{V_{C_1}}{L_1} + \frac{nV_{\text{in}}}{L_1} + \frac{\partial M_1}{\partial \hat{d}_1}\left(V_{C_1} + \frac{n^2 L_m}{L_1}\left(\left(r_{L_1} + r_{C_2}\right) I_{L_1} + V_{C_2} - r_{C_2} I_o\right)\right) \tag{52}$$

$$a_1 = C_1 C_2 r_{C_2} \frac{\partial F_3}{\partial \hat{d}_1} \tag{58}$$

$$a_2 = nC_1 \frac{\partial F_3}{\partial \hat{d}_1} - C_2 r_{C_2}\left(\left(I_{L_m} + nI_{L_1}\right)\frac{\partial F_3}{\partial \hat{x}_2} + nC_1\left(\frac{\partial F_3}{\partial \hat{d}_1}\frac{\partial F_1}{\partial \hat{x}_1} - \frac{\partial F_1}{\partial \hat{d}_1}\frac{\partial F_3}{\partial \hat{x}_1}\right)\right) \tag{59}$$

$$a_3 = -\left(I_{L_m} + nI_{L_1}\right)\frac{\partial F_3}{\partial \hat{x}_2} - C_2 r_{C_2}\left((1 - D_1)\left(\frac{\partial F_3}{\partial \hat{d}_1}\frac{\partial F_1}{\partial \hat{x}_2} - \frac{\partial F_1}{\partial \hat{d}_1}\frac{\partial F_3}{\partial \hat{x}_2}\right) + \left(I_{L_m} + nI_{L_1}\right)\left(\frac{\partial F_1}{\partial \hat{x}_2}\frac{\partial F_3}{\partial \hat{x}_1} - \frac{\partial F_1}{\partial \hat{x}_1}\frac{\partial F_3}{\partial \hat{x}_2}\right)\right)$$
$$+ nC_1\left(\frac{\partial F_1}{\partial \hat{d}_1}\frac{\partial F_3}{\partial \hat{x}_1} - \frac{\partial F_3}{\partial \hat{d}_1}\frac{\partial F_1}{\partial \hat{x}_1}\right) \tag{60}$$

$$a_4 = (1 - D_1)\left(\frac{\partial F_1}{\partial \hat{d}_1}\frac{\partial F_3}{\partial \hat{x}_2} - \frac{\partial F_3}{\partial \hat{d}_1}\frac{\partial F_1}{\partial \hat{x}_2}\right) + \left(I_{L_m} + nI_{L_1}\right)\left(\frac{\partial F_1}{\partial \hat{x}_1}\frac{\partial F_3}{\partial \hat{x}_2} - \frac{\partial F_1}{\partial \hat{x}_2}\frac{\partial F_3}{\partial \hat{x}_1}\right) \tag{61}$$

$$b_1 = nC_1 C_2 L_f \tag{62}$$

$$b_2 = nC_1 C_2\left(r_{C_2} + r_{L_f} - L_f\left(\frac{\partial F_1}{\partial \hat{x}_1} + \frac{\partial F_3}{\partial \hat{x}_3}\right)\right) \tag{63}$$

$$b_3 = nC_1 - C_2L_f\frac{\partial F_1}{\partial \hat{x}_2} - nC_1L_f\frac{\partial F_3}{\partial \hat{x}_4} + C_2D_1L_f\left(\frac{\partial F_1}{\partial \hat{x}_2} + n\frac{\partial F_3}{\partial \hat{x}_2}\right) - nC_1C_2\left(r_{C_2} + r_{L_f}\right)\left(\frac{\partial F_1}{\partial \hat{x}_1} + \frac{\partial F_3}{\partial \hat{x}_3}\right)$$
$$- nC_1C_2r_{C_2}^2\left(\bar{M}_1 + \bar{M}_2\right) + nC_1C_2L_f\left(\frac{\partial F_1}{\partial \hat{x}_1}\frac{\partial F_3}{\partial \hat{x}_3} - \frac{\partial F_1}{\partial \hat{x}_3}\frac{\partial F_3}{\partial \hat{x}_1}\right) \tag{64}$$

$$b_4 = (D_1 - 1)C_2\left(r_{C_2} + r_{L_f}\right)\frac{\partial F_1}{\partial \hat{x}_2} - nC_1\left(\frac{\partial F_1}{\partial \hat{x}_1} + \frac{\partial F_3}{\partial \hat{x}_2}\right) - nC_1r_{C_2}\left(\bar{M}_1 + \bar{M}_2\right)$$
$$+ (C_2L_f - C_2D_1L_f)\left(\frac{\partial F_1}{\partial \hat{x}_2}\frac{\partial F_3}{\partial \hat{x}_3} - \frac{\partial F_1}{\partial \hat{x}_3}\frac{\partial F_3}{\partial \hat{x}_2}\right) - nC_1r_{L_f}\frac{\partial F_3}{\partial \hat{x}_4} + nC_2D_1\frac{\partial F_3}{\partial \hat{x}_2}\left(r_{C_2} + r_{L_f}\right)$$
$$+ n^2C_1C_2\bar{M}_1r_{C_2}^2\frac{\partial F_3}{\partial \hat{x}_1} + nC_2D_1L_f\left(\frac{\partial F_1}{\partial \hat{x}_2}\frac{\partial F_3}{\partial \hat{x}_1} - \frac{\partial F_1}{\partial \hat{x}_1}\frac{\partial F_3}{\partial \hat{x}_2}\right) + nC_1L_f\left(\frac{\partial F_1}{\partial \hat{x}_1}\frac{\partial F_3}{\partial \hat{x}_4} - \frac{\partial F_1}{\partial \hat{x}_4}\frac{\partial F_3}{\partial \hat{x}_1}\right)$$
$$+ nC_1C_2\left(r_{C_2} + r_{L_f}\right)\left(\frac{\partial F_1}{\partial \hat{x}_1}\frac{\partial F_3}{\partial \hat{x}_3} - \frac{\partial F_1}{\partial \hat{x}_3}\frac{\partial F_3}{\partial \hat{x}_1}\right) + nC_1C_2r_{C_2}^2\left(\bar{M}_1 + \bar{M}_2\right)\frac{\partial F_1}{\partial \hat{x}_1} \tag{65}$$

$$b_5 = n^2C_1\bar{M}_1r_{C_2}\frac{\partial F_3}{\partial \hat{x}_1} + \left(nC_1\left(\frac{\partial F_3}{\partial \hat{x}_3} + r_{C_2}\left(\bar{M}_1 + \bar{M}_2\right) + r_{L_f}\frac{\partial F_3}{\partial \hat{x}_4}\right) - nC_2D_1\left(r_{C_2} + r_{L_f}\right)\frac{\partial F_3}{\partial \hat{x}_2}\right)\frac{\partial F_1}{\partial \hat{x}_1}$$
$$+ nC_2D_1\left(r_{C_2} + r_{L_f}\right)\frac{\partial F_3}{\partial \hat{x}_1}\frac{\partial F_1}{\partial \hat{x}_2} + nD_1\frac{\partial F_3}{\partial \hat{x}_2} - nC_1\left(\frac{\partial F_1}{\partial \hat{x}_3} + r_{L_f}\frac{\partial F_1}{\partial \hat{x}_4}\right)\frac{\partial F_3}{\partial \hat{x}_1} + nC_2\bar{M}_1r_{C_2}^2(1 - D_1)\frac{\partial F_3}{\partial \hat{x}_2}$$
$$+ (1 - D_1)\left(L_f\frac{\partial F_3}{\partial \hat{x}_4} + C_2\left(r_{C_2} + r_{L_f}\right)\frac{\partial F_3}{\partial \hat{x}_3} + C_2r_{C_2}^2\left(\bar{M}_1 + \bar{M}_2\right) - 1\right)\frac{\partial F_1}{\partial \hat{x}_2}$$
$$+ C_2(D_1 - 1)\left(r_{C_2} + r_{L_f}\right)\frac{\partial F_1}{\partial \hat{x}_3}\frac{\partial F_3}{\partial \hat{x}_2} + L_f(D_1 - 1)\frac{\partial F_1}{\partial \hat{x}_4}\frac{\partial F_3}{\partial \hat{x}_2} \tag{66}$$

$$b_6 = \left(\bar{M}_1r_{C_2}(1 - D_1)\frac{\partial F_3}{\partial \hat{x}_2} + D_1\left(\frac{\partial F_1}{\partial \hat{x}_2}\frac{\partial F_3}{\partial \hat{x}_1} - \frac{\partial F_1}{\partial \hat{x}_1}\frac{\partial F_3}{\partial \hat{x}_2}\right)\right)n + (D_1 - 1)\left(\frac{\partial F_1}{\partial \hat{x}_3}\frac{\partial F_3}{\partial \hat{x}_2} + r_{L_f}\frac{\partial F_1}{\partial \hat{x}_4}\frac{\partial F_3}{\partial \hat{x}_2}\right)$$
$$+ \left((1 - D_1)\frac{\partial F_3}{\partial \hat{x}_3} + r_{L_f}\frac{\partial F_3}{\partial \hat{x}_4} + r_{C_2}\left(\bar{M}_1 + \bar{M}_2\right) - D_1r_{C_2}\left(\bar{M}_1 + \bar{M}_2\right) - D_1r_{L_f}\frac{\partial F_3}{\partial \hat{x}_4}\right)\frac{\partial F_1}{\partial \hat{x}_2} \tag{67}$$

$$c_1 = n^2C_1C_2L_mV_{C_1} \tag{68}$$

$$c_2 = n^2L_m\left(C_1V_{C_1} - C_2D_1I_{L_1}r_{C_2}\right) - nC_2D_1I_{L_m}L_mr_{C_2} \tag{69}$$

$$c_3 = -n^2D_1I_{L_1}L_m - n(D_1I_{L_m}L_m + C_2r_{C_2}V_{\text{in}}D_1(D_1 - 1)) + C_2r_{C_2}V_{C_1}(1 - D_1) \tag{70}$$

$$c_4 = (nV_{\text{in}}D_1 + V_{C_1})(1 - D_1) \tag{71}$$

$$e_1 = n^2C_1C_2L_1L_fL_m \tag{72}$$

$$e_2 = n^2(r_{C_2}C_1C_2L_m(L_1 + L_f) + C_1C_2L_m(L_1r_{L_f} + L_fr_{L_1})), \tag{73}$$

$$e_3 = n^2L_m(C_2L_fD_1^2 + C_1(r_{C_2}C_2(r_{L_1} + r_{L_f}) + (L_1 + L_f + r_{L_1}r_{L_f}C_2))) + C_2L_1L_f(D - 1)^2 \tag{74}$$

$$e_4 = n^2L_m(C_1(r_{L_1} + r_{L_f}) + C_2D_1^2(r_{C_2} + r_{L_f})) + C_2(r_{C_2}(L_1 + L_f) + r_{L_1}L_f + r_{L_f}L_1)(D_1 - 1)^2 \tag{75}$$

$$e_5 = r_{L_f}r_{L_1}C_2(D_1 - 1)^2 + D_1(L_1 + L_f)(D_1 - 2) \tag{76}$$

$$e_6 = \left(r_{L_1} + r_{L_f}\right)(D_1 - 1)^2 \tag{77}$$

REFERENCES

[1] A. A. Hadi, U. Sinha, T. Faika, T. Kim, J. Zeng, and M. H. Ryu, "Internet of Things (IoT)-enabled solar micro inverter using blockchain technology," in *Proc. IEEE Ind. Appl. Soc. Annu. Meeting*, Sep. 2019, pp. 1–5.

[2] A. S. Mundada, Y. Nilsiam, and J. M. Pearce, "A review of technical requirements for plug-and-play solar photovoltaic microinverter systems in the United States," *Sol. Energy*, vol. 135, pp. 455–470, Oct. 2016.

[3] R. Hasan, S. Mekhilef, M. Seyedmahmoudian, and B. Horan, "Grid-connected isolated PV microinverters: A review," *Renewable Sustain. Energy Rev.*, vol. 67, pp. 1065–1080, Jan. 2017.

[4] O. Çelik, A. Teke, and A. Tan, "Overview of micro-inverters as a challenging technology in photovoltaic applications," *Renewable Sustain. Energy Rev.*, vol. 82, pp. 3191–3206, Feb. 2018.

[5] M. Uno and T. Shinohara, "Module-integrated converter based on cascaded quasi-Z-source inverter with differential power processing capability for photovoltaic panels under partial shading," *IEEE Trans. Power Electron.*, vol. 34, no. 12, pp. 11553–11565, Dec. 2019.

[6] H. Wu, X. Tang, J. Zhao, and Y. Xing, "An isolated bidirectional microinverter based on voltage-in-phase PWM-controlled resonant converter," *IEEE Trans. Power Electron.*, vol. 36, no. 1, pp. 562–570, Jan. 2021.

[7] B. Tamyurek and B. Kirimer, "An interleaved high-power flyback inverter for photovoltaic applications," *IEEE Trans. Power Electron.*, vol. 30, no. 6, pp. 3228–3241, Jun. 2014.

[8] T. Lodh, N. Pragallapati, and V. Agarwal, "Novel control scheme for an interleaved flyback converter based solar PV microinverter to achieve high efficiency," *IEEE Trans. Ind. Appl.*, vol. 54, no. 4, pp. 3473–3482, Apr. 2018.

[9] N. Falconar, D. Shekari, and M. Pahlevani, "An adaptive sensorless control technique for a flyback-type solar tile microinverter," *IEEE Trans. Power Electron.*, vol. 36, no. 12, pp. 13554–13562, Dec. 2020.

[10] M. A. Rezaei, K. J. Lee, and A. Q. Huang, "A high-efficiency flyback micro-inverter with a new adaptive snubber for photovoltaic applications," *IEEE Trans. Power Electron.*, vol. 31, no. 1, pp. 318–327, Jan. 2015.

[11] K. S. Kim, S. H. Lee, W. J. Cha, J. M. Kwon, and B. H. Kwon, "Bidirectional single power-conversion DC-AC converter with noncomplementary active-clamp circuits," *IEEE Trans. Ind. Electron.*, vol. 63, no. 8, pp. 4860–4867, Aug. 2016.

[12] C. C. Kuo *et al.*, "A dynamic resonant period control technique for fast and zero voltage switching in GaN-based active clamp flyback converters," *IEEE Trans. Power Electron.*, vol. 36, no. 3, pp. 3323–3334, Mar. 2020.

[13] S. H. Lee, W. J. Cha, B. H. Kwon, and M. Kim, "Discrete-time repetitive control of flyback CCM inverter for PV power applications," *IEEE Trans. Ind. Electron.*, vol. 63, no. 2, pp. 976–984, Feb. 2016.

[14] H. Kim, J. S. Lee, and M. Kim, "Downsampled iterative learning controller for flyback CCM inverter," *IEEE Trans. Ind. Electron.*, vol. 65, no. 1, pp. 510–520, Jan. 2017.

[15] R. Za'im, J. Jamaludin, and N. Abd Rahim, "Photovoltaic flyback microinverter with tertiary winding current sensing," *IEEE Trans. Power Electron.*, vol. 34, no. 8, pp. 7588–7602, Aug. 2018.

[16] R. C. Viero and F. S. dos Reis, "Dynamic modeling of a ZETA converter in DCM applied to low power renewable sources," in *Proc. IEEE Energy Convers. Congr. Expo.*, Sep. 2011, pp. 685–691.

[17] "How to properly evaluate junction temperature with thermal metrics," Texas Instrum., Dallas, TX, USA, Appl. Rep. SLUA844B, Mar. 2019.

[18] G. L. Piazza and I. Barbi, "New step-up/step-down DC-AC converter," *IEEE Trans. Power Electron.*, vol. 29, no. 9, pp. 4512–4520, Sep. 2013.

[19] M. S. Diab, A. Elserougi, A. S. Abdel-Khalik, A. M. Massoud, and S. Ahmed, "A Zeta-converter based four-switch three-phase DC-AC inverter," in *Proc. IEEE Energy Convers. Congr. Expo.*, Sep. 2015, pp. 4671–4677.

[20] K. K. H. Dia and M. A. Choudhury, "A single phase differential Zeta rectifier-inverter," in *Proc. IEEE Int. WIE Conf. Elect. Comput. Eng.*, Dec. 2015, pp. 284–288.

[21] R. K. Surapaneni and A. K. Rathore, "A single-stage CCM zeta microinverter for solar photovoltaic AC module," *IEEE Trans. Emerg. Sel. Top. Power Electron.*, vol. 3, no. 4, pp. 892–900, Apr. 2015.

[22] B. Han, J. Lai, and M. Kim, "Bridgeless Cuk-derived single power conversion inverter with reactive-power capability," *IEEE Trans. Power Electron.*, vol. 35, no. 3, pp. 2629–2645, Mar. 2020.

[23] S. Vighetti, J. Ferrieux, and Y. Lembeye, "Optimization and design of a cascaded DC/DC converter devoted to grid-connected photovoltaic systems," *IEEE Trans. Power Electron.*, vol. 27, no. 4, pp. 2018–2027, Apr. 2012.

[24] R. Yu, B. Pong, B. Ling, and J. Lam, "Two-stage optimization method for efficient power converter design including light load optimization," *IEEE Trans. Power Electron.*, vol. 27, no. 3, pp. 1327–1337, Mar. 2012.

[25] Y. Cho and J. Lai, "Digital plug-in repetitive controller for single-phase bridgeless PFC converters," *IEEE Trans. Power Electron.*, vol. 28, no. 1, pp. 165–175, Jan. 2013.

[26] Y. Wang, A. Darwish, D. Holliday, and B. W. Williams, "Plug-in repetitive control strategy for high-order wide-output range impedance-source converters," *IEEE Trans. Power Electron.*, vol. 32, no. 8, pp. 6510–6522, Aug. 2017.

[27] B. Han, J. Lee, and M. Kim, "Repetitive controller with phase-lead compensation for Cuk CCM inverter," *IEEE Trans. Ind. Electron.*, vol. 65, no. 3, pp. 2356–2367, Mar. 2018.

[28] B. Han, J. Lai, and M. Kim, "Dynamic modeling and controller design of dual-mode Cuk inverter in grid-connected PV/TE applications," *IEEE Trans. Power Electron.*, vol. 33, no. 10, pp. 8887–8904, Oct. 2018.

[29] B. Zhang, D. Wang, K. Zhou, and Y. Wang, "Linear phase lead compensation repetitive control of a CVCF PWM inverter," *IEEE Trans. Ind. Electron.*, vol. 55, no. 4, pp. 1595–1602, Apr. 2008.

Byeongcheol Han (Member, IEEE) was born in Busan, South Korea, in 1986. He received the B.S. degree in electrical engineering from Pusan National University, Busan, South Korea, in 2012, and the Ph.D. degree in creative IT engineering (CiTE) from the Pohang University of Science and Technology (POSTECH), Pohang, South Korea, in 2018.

In 2018, he was a Postdoctoral Researcher in CiTE with POSTECH. From 2018 to 2020, he was a Postdoctoral Associate with the Future Energy Electronics Center, Virginia Tech, Blacksburg, VA, USA. He is currently an Assistant Professor with the School of Electronics Engineering, Kyungpook National University, Daegu, South Korea. His research interests include nonlinear systems and control, grid-connected inverters, energy storage systems, and controller design for power conversion systems.

Seung-Won Jo (Student Member, IEEE) was born in Gwacheon, South Korea, in 1991. He received the B.S. degree in electronics and electrical Engineering in 2019 from Dongguk University, Seoul, South Korea, where he is currently working toward the M.S. degree in electronics and electrical Engineering.

His research interests include power conversion systems and control, grid-connected inverters, and renewable energy systems.

Nam-Gyeong Kim (Student Member, IEEE) was born in Asan, South Korea, in 1996. She received the B.S. degree in electronics and electrical engineering in 2020 from Dongguk University, Seoul, South Korea, where she is currently working toward the M.S. degree in electronics and electrical engineering.

Her research interests include power conversion systems and control, high-efficient power circuit design and bidirectional converter, and grid-connected inverters.

Jih-Sheng (Jason) Lai (Life Fellow, IEEE) received the M.S. and Ph.D. degrees in electrical engineering from the University of Tennessee, Knoxville, TN, USA, in 1985 and 1989, respectively.

In 1989, he joined the Electric Power Research Institute (EPRI) Power Electronics Applications Center (PEAC), where he managed EPRI-sponsored power electronics research projects. In 1993, he joined the Oak Ridge National Laboratory as a Power Electronics Lead Scientist, where he initiated a high power electronics program and developed several novel high-power converters, including multilevel converters and soft-switching inverters. In 1996, he joined Virginia Polytechnic Institute and State University. He is currently the James S. Tucker Professor with the Department of Electrical and Computer Engineering and the Director of the Future Energy Electronics Center. He authored/coauthored more than 450 refereed technical papers, one book chapter, two books, and 27 patents. His main research interests include high-efficiency power electronics conversions for high power and energy applications.

Dr. Lai was the recipient of the Technical Achievement Award in Lockheed Martin Award Night, 2 Journal Paper Awards, and 12 Best Paper Awards from IEEE sponsored conferences. He was the recipient of 2016 IEEE IAS Gerald Kliman Innovator Award. He led the student teams to win the Top Three Finalist in Google Little Box Challenge in 2016, Grand Prize Award from International Future Energy Challenge (IFEC) in 2011, and Grand Prize Award from Texas Instruments Engibous Analog Design Competition in 2009. He is the Founding Chair of 2001 IEEE IFEC and 2016 IEEE ACEPT, the General Chair of IEEE COMPEL-2000, IEEE APEC 2005, IEEE SPEC-2018, and IEEE IFEEC-2019 Conferences.

Minsung Kim (Senior Member, IEEE) was born in Ulsan, South Korea, in 1986. He received the B.S. and Ph.D. degrees in electrical engineering from the Pohang University of Science and Technology (POSTECH), Pohang, South Korea, in 2008 and 2013, respectively.

Since 2013, he has been with the Department of Creative IT Engineering and Future IT Research Laboratory, POSTECH, where he is currently a Research Assistant Professor. In 2016, he was a Research Scholar with the Future Energy Electronics Center, Virginia Tech, Blacksburg, VA, USA. In 2017, he also served as an Academic Visitor with Control and Power System Group, Imperial College London, London, U.K. Since 2018, he has been with the Division of Electronics and Electrical Engineering, Dongguk University, Seoul, South Korea, where he is currently an Assistant Professor. His current research interests include highly efficient power conversion circuit design, intelligent controller design for industrial electronics, and renewable energy and energy storage systems.